# INFORMATION AWARE FLIGHT PATH DESIGN FOR FLOW FIELD ESTIMATION AND PERFORMANCE INVESTIGATION OF ACTIVE FLOW CONTROL AIRCRAFT CONTROLLERS

By

ABDALRAHMAN KHALED MANSY

Bachelor of Science in Aerospace Engineering
Oklahoma State University
Stillwater, OK
2020

Bachelor of Science in Mechanical Engineering
Oklahoma State University
Stillwater, OK
2020

Submitted to the Faculty of the
Graduate College of the
Oklahoma State University
in partial fulfillment of
the requirements for
the Degree of
MASTER OF SCIENCE
December, 2022

INFORMATION AWARE FLIGHT PATH DESIGN FOR
FLOW FIELD ESTIMATION AND
PERFORMANCE INVESTIGATION OF
ACTIVE FLOW CONTROL AIRCRAFT CONTROLLERS

Thesis Approved:

Dr. Imraan Faruque

Thesis Advisor

Dr. Andy Arena

Dr. Ryan Paul

# ACKNOWLEDGMENTS

I would like to give an enormous thanks to my advisor Dr. Imraan Faruque. Words cannot describe how thankful I am for his guidance, expertise, and encouragement since undergrad. I will be forever thankful for his patience and support during my time as a graduate student, which has allowed me to advance my academic and professional career. I truly would not be where I am today without his help and guidance. I also want to extend my appreciation to my committee members, Dr. Andy arena and Dr. Ryan Paul, for all their help in classes and reviewing my thesis, and for providing their valuable feedback and time.

I am thankful to my friends and colleagues from APG. Special thanks to Ujjval Patel for supplying the base for the aircraft interpolation routine, as well as Christian Griffith and Christian Coletti for their work on the AFC pneumatic modeling and aircraft 6DOF simulator. I am forever grateful for the discussions had and the knowledge gained from all my colleagues in the lab and wish them the best in their future endeavors.

Finally, I would like to thank my family, my parents Dr. Khaled Mansy and Dr. Soha Elfeel, and my sister Reem for their love and support during my academic career. Nothing I have achieved would have been possible without them.

This work was supported in part by DARPA under `HR001104553` and the National Aeronautics and Space Administration under Grant `80NSSC20M0162`, University Leadership Initiative.

Acknowledgments reflect the views of the author and are not endorsed by committee members or Oklahoma State University.

Name: ABDALRAHMAN KHALED MANSY

Date of Degree: DECEMBER, 2022

Title of Study: INFORMATION AWARE FLIGHT PATH DESIGN FOR FLOW FIELD ESTIMATION AND PERFORMANCE INVESTIGATION OF ACTIVE FLOW CONTROL AIRCRAFT CONTROLLERS

Major Field: MECHANICAL AND AEROSPACE ENGINEERING

Abstract: This thesis discusses the feasibility and performance of implementing a COTS reciprocating piston compressor for a developed active flow control (AFC) actuation framework to quantify the aerospace-relevant performance ramifications of control architecture and compressor operational choices as well as the design and implementation of a systematic framework for specifying measurement trajectories for wind field structure system identification.

Three Active Flow Control architectures are studied under varying compressor operation schedules: supply volume metering (SVM), exit area metering (EAM), and a combined approach (VAM). The analysis framework in this study integrates internal pneumatic actuation and discharge dynamics, an experimentally-calibrated compressor pressure and thermal dynamics model, three feedback control architectures, and flight dynamics models. The framework is implemented in simulation to provide a user-friendly tool for linking AFC architecture choices to achievable flight trajectories. Actuator performance is evaluated using actuation time, output, compressor duty cycle, and specific energy consumption. Aircraft tracking performance is evaluated as usable time and slalom centerline deviation. The analysis indicates that exit area metering provides the best efficiency and run time with some structural drawbacks, while the combined approach provides the best flight-tracking performance at the expense of additional complexity.

This thesis also develops a systematic framework for specifying UAS-borne wind measurement trajectories based on information recovery. The framework quantifies information-richness in terms of wind field parameters and uses an initial flow structure estimate to construct a least squares optimization approach, including two alternative definitions of parameter information. The framework is implemented via dynamic programming within a flight dynamics and gust response simulator. The test cases include an isolated rotational (tornadic) flow structure and one embedded in a uniform wind field. The results indicate that an approach that optimizes based on observed flow gradients provides improved parameter estimate accuracy over one using only estimated flow structure gradients.

TABLE OF CONTENTS

LIST OF TABLES

LIST OF FIGURES

# CHAPTER I

# INTRODUCTION

## 1.1 Motivation

With technological advances in active flow control aircraft, implementation of such aircraft in the field is gathering interest. One area of implementation of interest is in stealth cases. Since AFC aircraft have no moving control surfaces, they are less detectable. A case where this may be needed is when an aircraft is being used to track a ship in the ocean by detecting disturbances in the flow field. For low observability, this action would need to occur while radar cross signature and radio communication links are reduced. This thesis has two main goals to support further work on this mission:

1. Determine optimal control architecture and operating conditions for an active flow control system with a commercial off-the-shelf (COTS) piston compressor
2. Develop a framework to determine the optimal flight path to estimate flow field parameters from wind field measurements

A COTS piston compressor is selected as the power supply of the aircraft to reduce cost and allow for more flexible propulsion options fo the aircraft.

To accomplish the goal of determining the optimal control architecture and operating conditions, this paper will

- Model compressor input to implement into AFC simulation
- Run simulations of different AFC configurations to compare the system performance
- Simulate the compressor with different operating conditions
- Simulate various flight maneuvers to test the aircraft's performance

In order to develop the framework to determine the optimal flight path estimate of a flow field's structure, this paper will also:

- Identify vortex flow field structure
- Determine influences on parameter estimation accuracy
- Formulate information term
- Develop agnostic optimization routine to guide aircraft flight path

Due to the computational complexity of modeling ship wake effects [11, 16], he flow field estimation routine will be tested with a simplified vortex model based on a model developed by Ash, Zuckerwar, and Zardadkhan.

### 1.2 Active Flow Control systems

Active flow control (AFC) has promised performance, maneuverability, and affordability [1, 17, 43, 49, 53] for various applications including aircraft and compressor/turbine design [24],

yet fielded aerospace systems have not realized the improvements seen in laboratory and wind-tunnel testing. One major reason is the comparatively high installed power requirements of AFC on the airframe. Contemporary AFC aircraft design work relies on experimental aerodynamics and computational fluid dynamics, both of which are relatively expensive ways to span the relatively large trade space needed for design studies. While laboratory aerodynamics experimentation and detailed computation examples have proven the principles [23, 26, 41, 42], efficient aerospace architecture and integration tools are crucial to enabling fielded systems like those in contemporary research programs such as DARPA's CRANE program. These tools include integrated simulation test environments and performance metrics to identify the performance sensitivities over the trade space and configurations and inform the choice of the most efficient AFC implementation architectures. These tools must incorporate concise mechanisms to evaluate the impact of design decisions, including component level modeling, discharge conditions, pressure regulation, and feedback, and an understanding of the important tools that can be used in rigorous robust control analysis and the ability to run real-time will provide hardware-in-the-loop simulation and human interoperability testing.

Despite the need, strong nonlinear coupling and interactions have complicated the search for efficient tools to predict the performance implications of AFC configuration choices. AFC is not well-suited to open loop control design due to these effects and a reduced order model supporting output feedback control will generally provide an improvement in AFC system controller [47] implementation. For complex systems like AFC implementations, producing a combined reduced order model may be involved, and if adequate performance may be reached via single-input-single-output controller design, controller design complexity could be significantly reduced. Accordingly, this study evaluates the performance of a distributed control system that implements three proportional feedback controllers, with limited coupling [48]. For the proposed AFC system, the compressor is controlled by a switch controller, while the valves and slots in the system are controlled by their respective

controllers.

To provide a conservative bound on AFC configurations, this study uses a mass-flow demanding circulation control approach using the Coanda effect to impart momentum into the flow to delay flow separation [50]. The system performance sensitivity regarding mass flow power consumption is investigated about the control metering and compressor controller choice. AFC systems having a dedicated or separate compressor are notorious for mass flow generation being the dominant (90%) AFC power demand [10, 21].

### 1.3 Flow field estimation framework

Tornados remain a highly unpredictable dynamic event associated with convective supercells, characterized by large velocity gradients and very localized structures that can cause significant human and structural damage. While current radar-based weather forecasting can indicate likely regions for tornado formation, the actual event happens suddenly and human observation remain the primary tool for estimating the size, severity, and trajectory of the tornado. The lack of forecast ability is due to both limitations on measurement and forecasting. Radar-based measurements sense moisture, and not all tornados are rain wrapped. The complex multi-scale physics involved in tornado formation and relatively limited knowledge about tornado dynamics further increase uncertainty in real-time tornado localization and structure determination. New methods such as infrasound detection and tracking are being developed to increase the prediction capabilities of weather forecasting, however, the bulk of forecasters must continue to rely on human stormchasers for direct observation of tornadic conditions. The ability to localize and estimate tornadic structures from onboard unmanned aerial systems (UAS) operating in the area would provide a mechanism to reduce the need for human stormchasing observers in the area of dangerous weather. UAS-borne atmospheric measurement efforts have led to dynamic measurements of local pressure,

temperature, humidity, and wind conditions. Current convective supercell measurement campaigns generally rely on UAS trajectories designed by human choices, such as compliance with legacy measurements such as vertical sounding profiles, mission planning conveniences such as the racetrack or "lawn-mower" paths, or intuition such as flying towards observed dynamic events. Integration of UAS-borne measurements into the weather forecasting enterprise will benefit from a more disciplined approach to recovering maximal information about the flow structure, especially for large numbers of coordinated vehicles.

This paper develops an information-aware flight path planning framework to support efficiently estimating the structure of wind motions from a UAS inferring local wind conditions from small-scale disturbances. This approach is based on defining an integral-based notion of path information, and incorporating that with gust response models and a dynamically-refined flow structure estimate. The performance is quantified in a dynamic wind field and flight simulator incorporating a quasi-steady model of a rotating tornadic event embedded in a steady wind. The results provide a direct comparison of the flow field structure and its parameter uncertainties.

### 1.3.1 Wind inference algorithms

Wind interactions that disturb objects in the environment can be estimated by quantifying the disturbance of the aircraft due to gusts [7]. This concept can be applied to aircraft, where the difference between the aircraft's measured and modeled motion is assumed to be the gust response and inverted to estimate the local wind conditions [44, 45].

### 1.3.2 System identification and applied information theory

System identification frameworks have been applied to flow velocities in water to identify the source and sink singularities in a flow via Least Squares [38]. Least squares can be effective in parameter estimation for nonlinear models, as it reduces the reliance on an established state space model. The framework discussed in this paper utilizes a similar parameter estimation routine, discussed in [30], which utilizes Least Squares Regression. This method minimizes the error between measured and estimated states to identify the flow field parameters. Information theory is applied to the system identification of the flow field to improve the parameter estimation. Having a more informative model leads into have higher certainty in the flow field system identification. The more informative a data set is, the more it is capable of being distinguishable from different models [28].

### 1.3.3 Wind field modeling

This study primarily modeled vortex flows, concentrating on those that are receiving the most attention in tornado physics identification. Recent work has compared the potential vortex, Burger's vortex, and the Ash, Zuckerwar, and Zardadkhan (AZZ) vortex model, which incorporates pressure relaxation into the vortex structure, causing velocities in the structure to initially grow with increasing radius and then decay beyond a peak velocity [3]. The model's agreement growing across multiple domains [4] makes AZZ the assumed vortical structure in this study. Vertical variation is still not well addressed in concise tornadic vortex models, and this study uses a two-dimensional (planar) wind field to focus on the system identification and data information aspects.

## 1.4 Thesis Structure

The rest of this thesis structure is as follows: the performance study on the AFC system is discussed in chapter 2. The system architectures are discussed, looking at the different configurations as well as defining the maneuvers to evaluate the system performance. With AFC system defined and discussed, the next two chapters focus on the system identification and information flight path frameworks. Chapter 3 looks into how the flow fields were modeled and simulated as well as investigates the parameter estimation framework for an isolated tornado flow structure using predetermined flight paths. With this framework established and some baseline results, chapter 4 then defines the framework for using information from the flow field structure to guide the aircraft's flight path.

# CHAPTER II

# AFC AIRCRAFT PERFORMANCE STUDY

## 2.1 Active flow performance in aircraft

While considerable work quantifies active flow control performance in a laboratory environment [23,41], the limited number of flight-tested configurations constrains the availability of aircraft-specific measurements. The most common design for AFC systems includes using the bleed air from the compressor in the engine to supply the air and mass flow required for the system, as seen in [14, 20, 55]. For the example in Crowther [55], a small-scale UAS was designed with an implemented AFC system that used the bleed air from the engine to provide control for trim and flight maneuvers in place of traditional control surfaces. However, these methods can be wasteful, as when the aircraft is not utilizing the bleed-air, it is dispelled into the ambient flow and not stored in a tank for later use. System operation negatively affects engine performance, with aircraft thrust reductions of up to 7% for a modest bleed flow of 2.6% [14]. These negative performance transients require the AFC and flight control systems to account for powerplant performance degradation. Additionally, the usage of bleed airflow is limited to the engine temperature limits. Using a higher percentage of bleed flow increases the temperatures seen by the turbine for turbojet powerplants, and must thus be relegated carefully. For instance, a full-sized transport aircraft can maintain max bleed flow safely for 8 minutes, as observed by Hemmerly [20]. With these constraints, it is important to explore

and evaluate different AFC systems that can store air for future use and that put as little strain as possible on the aircraft powerplant.

## 2.2 Compressor modeling

Three main compressor types power onboard AFC systems: scroll, rotary vane, and reciprocating piston compressors. Scroll compressors typically have a higher efficiency than rotary compressors for small-medium scale use, while rotary compressors are more effective for larger scale settings [22,35,52]. A scroll compressor's high sensitivity changes in air temperature and composition make the design most effective at a specific operating condition [12,27,54], which is limiting for an AFC system experiencing relatively rapid charge and discharge transients. The achievable compressor output lapses with altitude [46] (e.g., typically a 20% reduction at 3000m) as the efficiency decreases due to increased pressure ratio [29,32,39], an effect further reducing output.

Vane compressors generally achieve a higher efficiency than piston counterparts due to leakage losses in the piston/cylinder interface [5,51]. For the piston compressors, the rolling compressor offered a higher coefficient of performance (COP) at all operating conditions in a heat pump application relative to the reciprocating piston; the average COP increase has been measured at 10% [13].

The lower efficiency of a piston compressor is somewhat mitigated by the wide range of operating conditions and significantly reduced airframe integration challenges. Inexpensive compressors with a sufficient weight to CFM output ratios are commercially available. Proving the feasibility of implementing a piston compressor could significantly reduce the financial costs and implementation complexities of realizing an AFC system for UAS.

## 2.3 Active flow control modeling and simulation

This project builds on the pneumatic dynamics developed in [18, 19], where three valve and exit area meterings were considered for the internal pneumatic structures of an AFC system and reduced order models developed for open and closed-loop responses of the actuation concepts, characterizing actuation performance during discharge from a pre-charged tank condition (i.e., no operational compressor).

The current study expands on previous work [8, 18, 19] by integrating an onboard compressor model based on polytropic modeling and experimental testing on a commercially-available piston compressor. This study also integrates the AFC actuation (including the compressor) with a flight dynamics simulation to provide a mechanism to assess in-flight performance assessment for two mission task elements.

## 2.4 System Modeling

The aircraft's onboard pneumatic system consists of a compressor, a supply tank, and a discharge plenum in each wing as illustrated in Fig. 1, capable of supply valve and exit area metering.

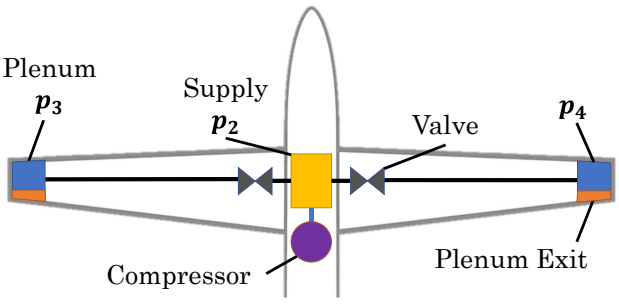


Figure 1: Active Flow Control system Layout

Pneumatic modeling consists of a compressor, tank volumes, pneumatic lines, and valve components. This study integrates the effects of compressor operation, and the other

components are consistent with [18]. An implemented simulator provides an output $C_\mu$ based on the desired input $C_\mu$, and 6DOF flight simulator is integrated to provide trajectory study capability.

### 2.4.1 Pneumatic modeling

#### Compressor

The compressor selected for the system is the XD4000-24, a continuous-duty cycle compressor manufactured by Oasis. It is a direct current portable piston compressor. The specifications for the compressor are shown in Table 1, referenced from [34].

| | |
|---|---|
| **Type** | Single-stage piston |
| **Output** | 8 CFM @90psi |
| **Max pressure** | 200 psi |
| **Power** | 2.2 hp |
| **Weight** | 65 lb |

Table 1: XD4000-24 Compressor Specifications

We applied a polytropic efficiency compressor model [40], in which the compressor outputs a mass flowrate $\dot{m}$ as a function of power required $\dot{W}$, as

$$\dot{W} = \eta \dot{m} \frac{nRT_1}{n-1} \left[ \left( \frac{p_2}{p_1} \right)^{\frac{n-1}{n}} - 1 \right], \tag{2.4.1}$$

where ambient pressure $p_1$ and temperature $T_1$, the polytropic index $n$, and universal gas constant $R$ are considered fixed. The supply tank pressure $p_2$ represents the discharge pressure for the compressor and constraints output.

The compressor polytropic efficiency for this system is extrapolated from experimental data to capture the change in compressor efficiency as the downstream pressure changes. To

accomplish this, the density change over time is calculated as a function of the discharge pressure $p_2$, followed by the change in mass to calculate the mass flowrate seen in the experiment via

$$\rho = \frac{p_2}{RT} \tag{2.4.2}$$

$$m = \rho V \tag{2.4.3}$$

$$\dot{m}(t) = \frac{\Delta m(t)}{\Delta t}, \tag{2.4.4}$$

since a mass flow sensor could not be placed at the compressor outlet.

Assuming that the compressor operates at its rated power $\dot{W}$ continuously, Eqn. (2.4.1) can be rewritten as a function of pressure ratio and mass flowrate

$$\eta = \frac{\dot{m}}{\dot{W}} \frac{nRT_1}{n-1} \left[ \left( \frac{p_2}{p_1} \right)^{\frac{n-1}{n}} - 1 \right]. \tag{2.4.5}$$

The compressor efficiency is modeled as a second-order polynomial based on experimental testing quantifying the pressure ratio increase within a closed container, discussed in Section 2.5. The mass flowrate may then be isolated to be a function $f(p_2/p_1)$ of the pressure ratio only by rearranging Eqn. (2.4.1) to be

$$\dot{m} = \eta \dot{W} \left( \frac{nRT_1}{n-1} \left[ \left( \frac{p_2}{p_1} \right)^{\frac{n-1}{n}} - 1 \right] \right)^{-1}. \tag{2.4.6}$$

### Pneumatic model verification

To verify the model performance, a charging experiment was implemented with the compressor connected to an air tank as seen in Fig. 2. The experimental setup measures the compressor head/nozzle temperature $T_{no}$, the supply tank pressure $p_2$, supply tank air temperature $T_2$, and incorporated a mass flow sensor to measure the discharged air mass-flow $\dot{m}_{out}$. The experiment charged the tank from empty to operational pressure (0 to 180psi).

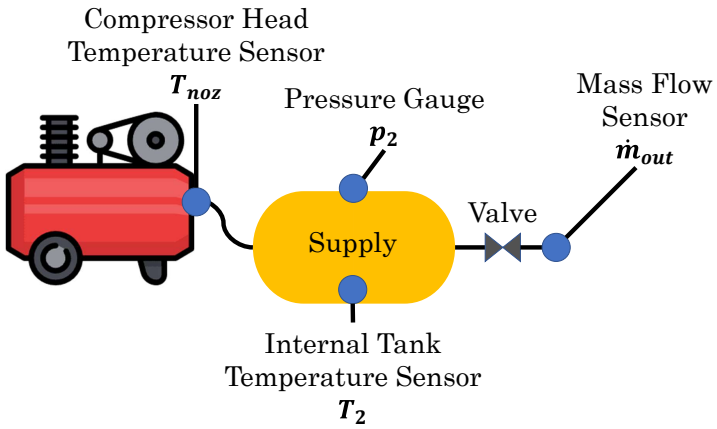


Figure 2: Experimental Setup

The nozzle temperature was modeled and compared to the experimental data. The physical experiment measured the nozzle temperature rather than the direct air temperature. The compressor nozzle temperature was modeled as a convective heat transfer system [25, 36] as

$$C_{no}\frac{dT_{no}}{dt} = \frac{T_2 - T_{no}}{\Phi_{in}} - \frac{T_{no} - T_1}{\Phi_{out}} \tag{2.4.7}$$

$$C_{no} = \rho_{no} V_{no} c_{p,no} \tag{2.4.8}$$

$$\Phi = \frac{1}{hA}, \tag{2.4.9}$$

where $C_{no}$ is the compressor nozzles thermal capacitance, $T_2$ is the air temperature discharged by the compressor, $T_1$ is the ambient temperature, and $\Phi_{in}$ and $\Phi_{out}$ are the thermal

resistances of the inner and outer nozzle surfaces, respectively. The nozzle head was composed of aluminum and the convection was assumed to be forced within the nozzle and free on its exterior. The tank internal temperature was assumed to be constant and equal to the system suction air temperature, or the compressor discharge air temperature. The assumptions' validity will be discussed in Section 2.5.

The compressor output pressure was also modeled as described in [31]. The discharge pressure is the supply tank pressure and is modeled via

$$\frac{p_2}{t} = \frac{m}{t}\frac{RT_1}{V_{sup}} = \frac{\dot{m}RT_1}{V_{sup}}. \tag{2.4.10}$$

Equation (2.4.10) relates $p_2$ to the output mass flowrate $\dot{m}$ and supply tank volume $V_{sup}$. The predicted pressure was compared with the experimental results.

### 2.4.2 Pneumatic control configurations

Three variations of the AFC system were compared to assess the effect of valve and exit area meterings. The configurations are supply valve metering (SVM), exit area metering (EAM), and both valve and area metering (VAM). The meterings control the open area $A$ of the valves and slots in the system, and are summarized in Table 2.

| Test Configuration | Supply valve | Exit area |
|---|---|---|
| SVM | P control | Fixed |
| EAM | Fixed | P control |
| VAM | P control | P control |

Table 2: Valve Control Configuration for Pneumatic Simulator

The SVM approach holds the exit areas (plenum openings) constant while the supply tank valves are controlled by a proportional controller ("P control"), where the input signal is the

$C_\mu$ error, and the exit signal is the supply valve area $A_2$.

The EAM concept holds the supply tank valves area constant while the plenum exit slots are controlled by separate P controllers, where the input signal is the same $C_\mu$ error from SVM and the output signal is the slot exit areas $A_3$ and $A_4$ for the starboard and port plenums, respectively.

The VAM approach maintains the plenums at a constant pressure by adjusting all the system valve areas. The supply tank valves are controlled by a P controller, where the signal input is the error between the starboard plenum pressure $p_3$ and the target plenum pressure $p_{id}$ of 30 psig. The exit slots are controlled by a P controller acting to minimize the error between the input and output $C_\mu$.

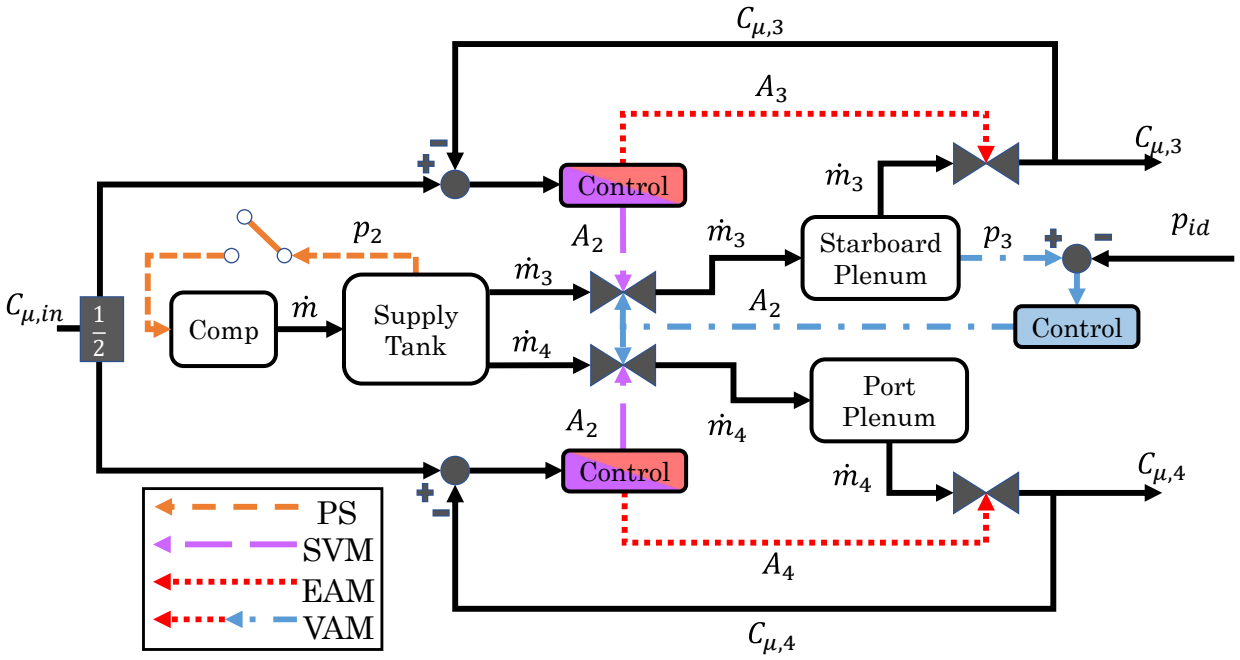


Figure 3: Pneumatic system and the three actuation metering concepts studied.

### 2.4.3 Compressor controller

Each configuration includes a binary compressor control based on a pressure switch activating the compressor once a set supply tank pressure $p_2$ is reached, as shown in Fig. 3. Four cut-in pressures (30, 60, 120, and 180 psig) were tested for the pressure switch to quantify the effect of cut-in pressure on system performance. The pressure range covers the nominal plenum pressure through maximum tank operational pressure.

### 2.4.4 Flight dynamics modeling

#### Construction

Flight maneuvers were modeled using the 6DOF simulator discussed in [8]. The simulator utilizes the lateral and longitudinal aircraft dynamics detailed in [33] with aircraft force and momentum coefficients determined using the linear design method in [6].

The simulator receives joystick inputs for the Euler angles (pitch, yaw, and roll) and throttle, which are then used as inputs for the pneumatic system to calculate the system output $C_\mu$. The equations used to model the pneumatic system were derived from [9] and are discussed in [18]. These equations calculate the mass flow and pressure losses due to the valve fittings and system ducting effects. Based on the achieve $C_\mu$ output, the simulator computes the integrated aircraft position and orientation.

**Airframe example and flight maneuvers**

The simulator incorporated the AFC system into a group 3 UAS aircraft. The aircraft specs are shown in Table 3.

| | |
|---|---|
| **Wingspan** $b$ | 47.5 ft |
| **Chord** $c$ | 5.7 ft |
| **Weight (MTOW)** | 1700 lbf |
| **Powerplant** | Continental O-200 |

Table 3: Aircraft Specifications

The aircraft's ailerons were replaced with the proposed AFC system as in Fig. 1. The integrated onboard compressor feeds the supply air tank, which supplies the mass-flow to the plenums, and controls this flow through the use of valves on the tank exit. The plenums receive the mass flow from the supply tank and control the discharged air by adjusting the plenum exit area.

The AFC system weight breakdown is listed in Table 4. The system total weight is 122 lbs, which includes the system components and fittings.

| **Component** | **Weight, lb** |
|---|---|
| **Compressor and Power Supply** | 95 |
| **Tank** | 10 |
| **Ducting** | 7 |
| **Plenum** | 10 |

Table 4: AFC System Weight Breakdown

The aircraft was subjected to two flight maneuvers. The first maneuver was a step maintaining a max roll input, corresponding to 95% max $C_\mu$ achievable by the aircraft. The other maneuver tested was a continuous slalom maneuver, where the input $C_\mu$ was sinusoidal, with amplitude at 50% max $C_\mu$ achievable by the system. The $C_\mu$ inputs were held until the supply tank pressure was depleted and maintained during compressor cycling to assess compressor duty cycle and achievable flight trajectories.

### 2.4.5 Performance quantification

#### Actuator performance

Some figures of merit must be defined to properly compare the different test configurations results. The actuator figures of merit are related to the directional $C_\mu$ system output, and consist of rise time $t_r$, actuation time $t_a$, energy consumed $E_{in}$, power efficiency (duty cycle) $D$, integrated ("total") $C_\mu$, and power-specific $C_\mu$.

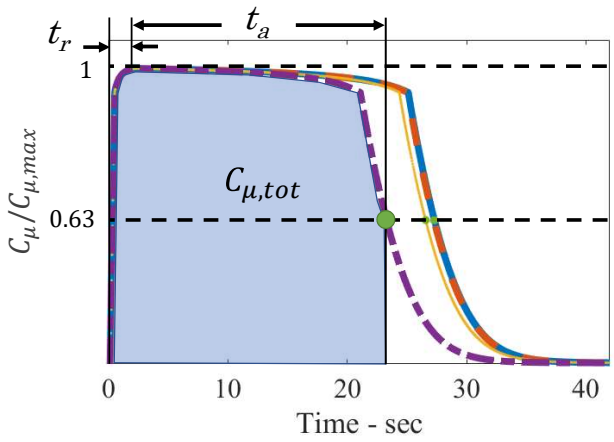


Figure 4: Performance Metrics Definitions

**Actuation time response** Two parameters were used to quantify the actuation time dynamics. Rise time $t_r$ is defined as the time to reach approximately 86% of the desired input $C_{\mu,in}$. Actuation time $t_a$ is defined as the time that the output $C_\mu$ stays above the "useful" or minimum $C_\mu$ output for the maneuver, $C_{\mu,min}$.

**Actuator output magnitude** "Useful $C_\mu$" is defined as approximately 63% $C_{\mu,in}$. The total $C_\mu$ is defined as

$$C_{\mu,tot} = \int C_\mu \quad dt,$$

and quantifies the directional $C_\mu$ response integrated area.

**Energy and power consumption** The duty cycle $D$ is defined as

$$D = \frac{t_c}{t_a},$$

or the percentage of time the compressor is operational during the full actuation period. The continuous duty compressor does not require a rest period, however, the percent of time the compressor is operating directly translates to power consumed, and duty cycle serves to quantify this effect. Because head temperature rises to an asymptote during operation and mass flow output is reduced at high temperature, reducing the duty cycle can also improve efficiency. The duty-cycle was quantified over three actuation periods under a commanded $C_{\mu,max}$ and normalized by that configuration's actuation time.

The specific $C_\mu$, denoted by $\overline{C_\mu}$, is defined as

$$\overline{C_\mu} = \frac{C_{\mu,tot}}{\dot{W} t_c}, \tag{2.4.11}$$

and quantifies the ratio between the total $C_\mu$ produced by the compressor and the total energy consumed by the compressor at max CFM output.

**Mission-specific performance**

**Max roll input** The max roll input bank case modeled the aircraft at the maximum roll input to observe the aircraft performance when outputting maximum $C_\mu$. 95% of the maximum achievable momentum coefficient $C_{\mu,max}$ was used as the input signal for desired momentum coefficient $C_{\mu,in}$. The aircraft maneuver was held until the output $C_\mu$ reached $0.63C_{\mu,max}$, resulting in the useful $C_\mu$ encompassing the shaded region in Fig. 4.

**Slalom maneuver** The slalom maneuvers were conducted commanding a cosine input. The input signal amplitude was set to half of the max roll input to maintain a stable sustained slalom in the 6DOF simulator as seen in Fig. 5.

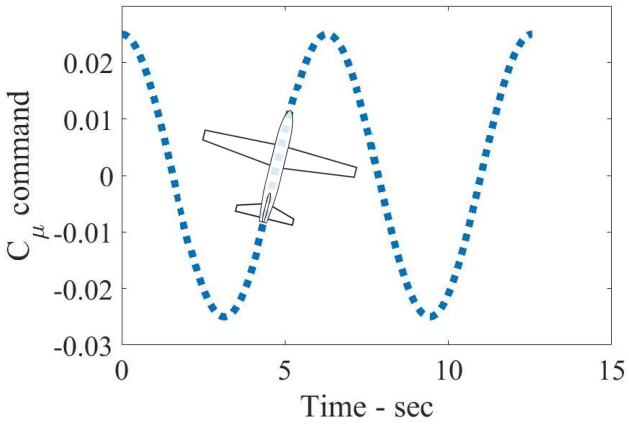


Figure 5: Slalom Maneuver Command

The yaw and pitch inputs were held at constant, and the throttle for the aircraft was set to 75% of the max throttle input to maintain directional stability for the aircraft.

The roll stick input had an amplitude of half the maximum bank input (50% roll). Additionally, a period of $\frac{\pi}{12.5}$ was selected for the s turns, with the resulting roll input proportional to

$$C_{\mu,in} = 0.5 C_{\mu,max} \cos\left(\frac{\pi}{12.5} t\right). \tag{2.4.12}$$

To quantify the aircraft trajectory performance, the aircraft's slalom centerline drift $d$ with a depleted supply tank was calculated as the distance between the actual flight path $X$ after compressor activation and the linear trajectory for the duration of compressor usage, defined as the slalom centerline $CL$ via

$$d = \sum_{t=t_c}^{t_f} \min\left(X(t) - CL\right). \tag{2.4.13}$$

## 2.5 Pneumatic model verification

Figure 6 shows the experimentally quantified efficiency ratio. The experiments indicate the compressor reaches a maximum efficiency near a pressure ratio of 7.5, or a supply tank pressure of 100 psig. A second-order polynomial fit was used to provide a functional description of the behavior as

$$\eta = -0.0093 \left(\frac{p_2}{p_1}\right)^2 + 0.1462\frac{p_2}{p_1} + 0.073. \tag{2.5.1}$$

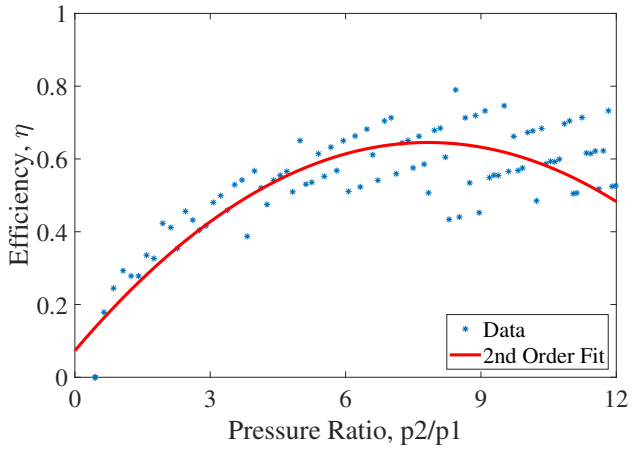


Figure 6: Compressor Efficiency, $\eta$ vs Pressure Ratio

The resulting compressor efficiency curve performs similarly when compared to experimental data, as seen in Fig. 7, where a 4.2 cubic foot tank is charged from 0 to 180 psig in experiment and simulation. The significant pressure transients in Fig. 7 influenced the decision to not implement isentropic modeling of the internal pressures in the AFC system.

While the model underpredicts performance in the higher pressure regimes ($> 90$ psig), the peak errors were less than 10%, which was sufficient to resolve the differences seen in the following actuator and flight performance assessment sections.

The experimental nozzle temperature record is shown in Fig. 8 and shows the variations

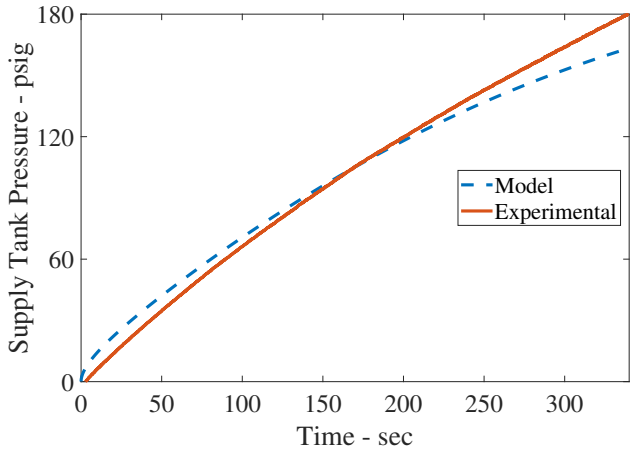

Figure 7: Compressor Tank Charging

between the model and experimental nozzle temperature data. The model and experiment deviation is likely related to the assumption that the forced convective heat transfer coefficient is constant. The heat transfer coefficient for a pressurized system varies as the system pressure changes, as discussed in Gao [15]. The model's discharge air temperature becomes

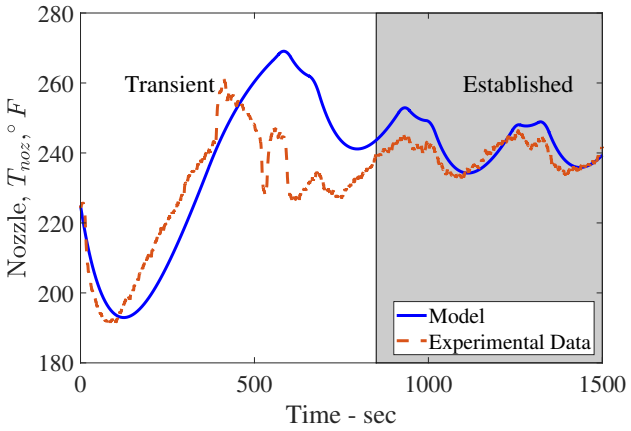

Figure 8: Temperature comparison

established after the first few charge and discharge cycles and begins to more closely follow the experimental data. The internal air temperature increased by a maximum of $30^\circ F$ during 75 minutes of continuous charge and discharge. There was a 10% increase in tank temperature for the charging session alone. The 6 psi average pressure deviation and nozzle temperature's maximum deviation of 7°F in the established operation was sufficient to establish trends in the system's performance.

## 2.6 Flight Maneuver Results

### 2.6.1 Max Roll Input

The max roll input maneuver was used to understand the baseline AFC actuation performance and observe the variations due to the different valve meterings at the most extreme roll case, where the system would be at its highest demand. The aircraft experiences aggressive roll and negative pitch until the tank is depleted and the compressor is utilized, allowing for the aircraft to perform a descending loiter.

#### Rise Time and Actuation Time

The achieved $C_\mu$ curves for the different valve meterings are shown in Fig. 9, showing that EAM maintains discharge for significantly longer than SVM, and marginally longer than VAM.

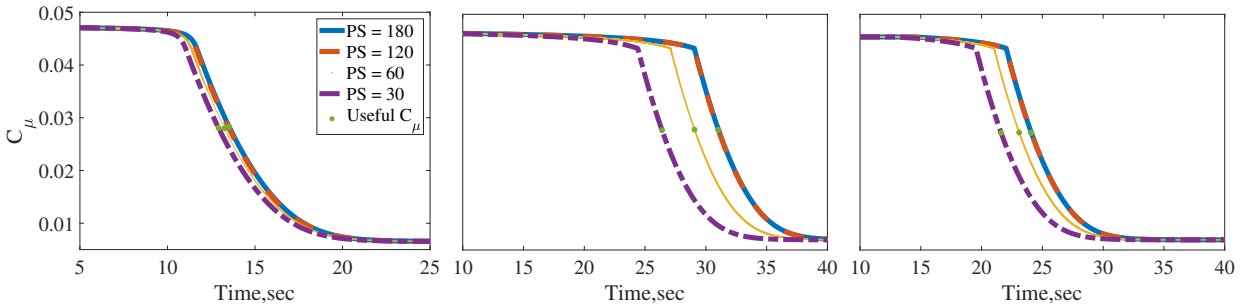


(a) SVM (b) EAM (c) VAM

Figure 9: Achievable $C_\mu$ curves over time.

The differences due to compressor cut-in pressure are less significant and are strongest in the decaying $C_\mu$ region of EAM. This lack of separation between the cut-in pressures may be attributed to the tank pressure decreasing rapidly until either the desired pressure in the plenum is reached or matches the pressure in the supply tank. This phenomenon would

explain the actuation time equivalence of the cut-in pressures above 120 psi.

Figure 10 shows VAM achieves the fastest rise time and SVM the longest. Rise time does not change significantly between cut-in pressures, suggesting the rise time is limited by the airspeed itself within the pneumatic system and the compressor operation is independent of the directional $C_\mu$ rise time.

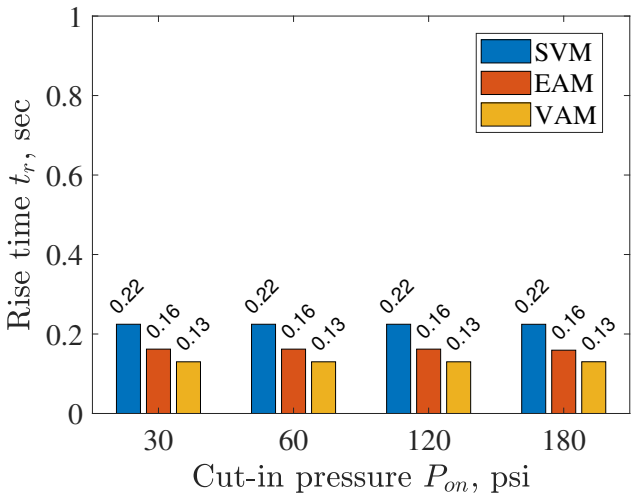


Figure 10: Rise time

Figure 11 shows actuation time is influenced by the compressor operation. Actuation time

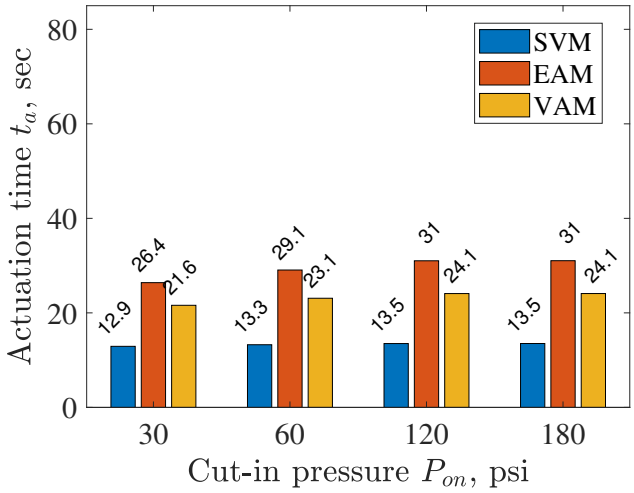


Figure 11: Actuation time

increases with cut-in pressure in a nonlinear fashion with decreasing slope. The diminishing

returns with increasing cut-in pressure may be related to the compressor operating at pressures higher than the ideal pressure ratio.

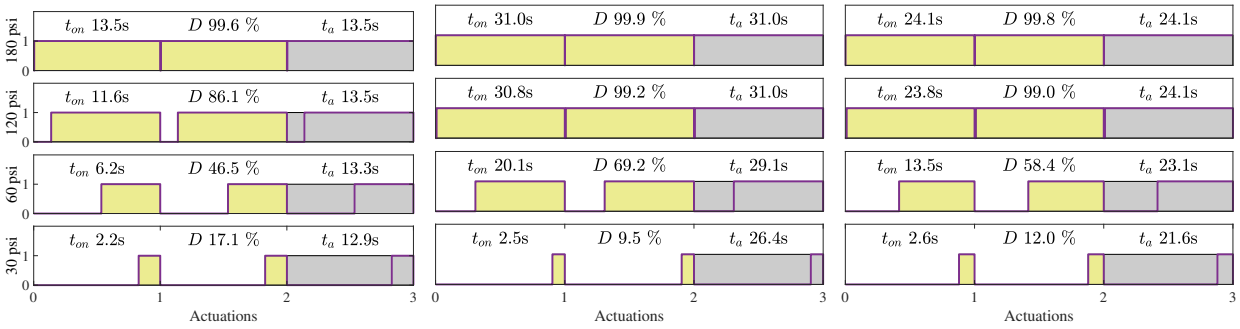


Figure 12: Compressor on/off operation time distribution

**Power**

The power consumed by the compressor can help guide power source selection, which could have a significant effect on airframe endurance. Figure 12 shows that SVM achieves the lowest compressor duty cycles and EAM the highest, an important finding for duty-cycle limited compressors. This finding means that the compressor is used proportionally less in the SVM configuration than the other configurations during system actuation. This reduction in compressor usage comes at the cost of limited actuation time, as SVM provides about half the actuation time as the other configurations. This result means that if a maneuver will not be sustained for an extended time period, SVM may provide better power efficiency than EAM and VAM. EAM prolongs actuation at the cost of higher compressor usage. The VAM case trades off actuation time for lower compressor usage, with a 20% decrease in actuation time for lower compressor usage. The decreased compressor usage depends on the cut-in pressure selected for the system. The duty cycle changes significantly between the 30 and 60 psi cut-in pressures, with significantly less variation between the 180 psi and 120 psi switch cases, suggesting there is no increased benefit to operating the compressor at higher supply tank pressure. Between the three valve control configurations, the pressure switch case with the highest disparity between them is when the cut-in pressure is close to 60 psi, a trend

consistent with the actuation time results.

The duty cycle decreases in a nonlinear way as the compressor cut-in pressure is decreases. In the VAM case, the change from 180 psi to 120 psi results in a 0.8 percent decrease, while the change from 120 psi to 60 psi is 36.2% percent decrease.

To illustrate how cut-in pressure affects the duty cycle for the three valve meterings, Fig. 13 shows the duty cycle percentages for this system at cut-in pressures from 30 psi to 180 psi. Three distinctive trends are observed consistent with the previous observation that the compressor duty cycle trend is strongly affected by the system valve meterings. From Fig. 13, we see that EAM has the most dramatic increase in duty cycle, SVM with slowest increase, and VAM as the balanced metering. The VAM system follows the same trend as the EAM metering for the lower cut-in pressures (less than 45 psia), then changes slope and follows the same slope as the SVM metering to until it reaches max duty cycle. The VAM configuration is influenced more by the EAM metering when the supply tank nears depletion, and becomes more dominated by the SVM metering while the supply pressure is higher than the plenum pressures. The VAM concept generally operating in a region bounded by the other two concepts is consistent with it combining control strategies from both supply valve and exit area metering. This duty cycle trend means that the VAM metering, which provides more than 70% increase in actuation time than SVM, has a much more flexible range of cut-in pressures where the compressor is not run continuously for the entire actuation than EAM.

Figure 14 shows that total $C_\mu$ directly correlates with actuation time and the compressor switch on pressure. When the compressor turns on at higher tank pressure ratios, the full system actuation time is increased. The total $C_\mu$ generated by the compressor sees a sharp decrease as the cut-in pressure approaches ambient pressure. This effect reflects a decrease in compressor operation time and reduction in mass flow input.

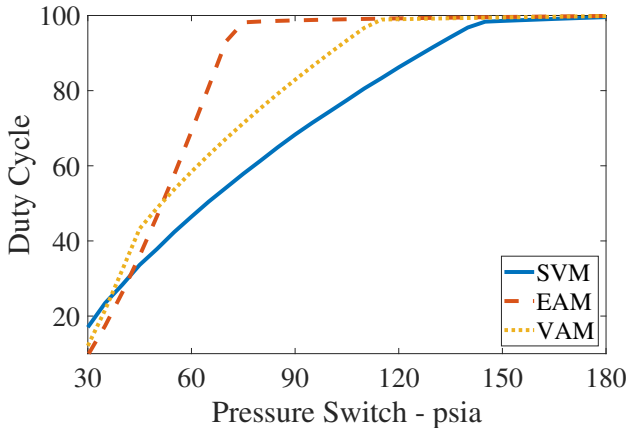


Figure 13: Duty cycle is affected by configuration and $P_{on}$.

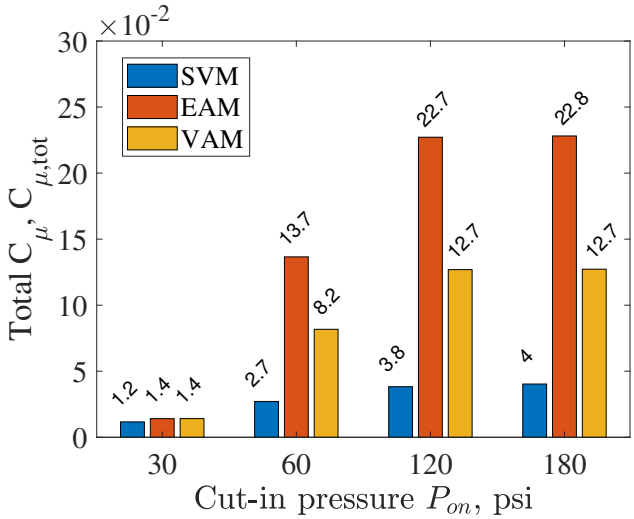


Figure 14: Total Momentum Coefficient, $C_\mu$

The power-specific momentum coefficient $\overline{C_\mu}$ does not follow the same trend. For the SVM metering, we see in Fig. 15 that the specific momentum coefficient decreases as cut-in pressure increases, and vice-versa for the EAM metering. The VAM metering increases and then decreases, following a parabolic trend with increasing cut-in pressure, peaking around the 60 psi cut-in pressure range. This behavior is significant as it is consistent with the results from the duty cycle discussion that there is little benefit for operating the compressor at higher cut-in pressures, where there is a no increase in specific $C_\mu$ for the VAM and a 6.5% and 3% decrease for SVM and EAM respectively, and the cut-in pressures near the compressors ideal pressure ratio provide the best performance for EAM and VAM.

Although the changes seem to be small for the max roll input case, as the input for roll decreases, the disparity between the valve meterings and cut-in pressures increases as there is less demand on the system to impart momentum into the airflow.

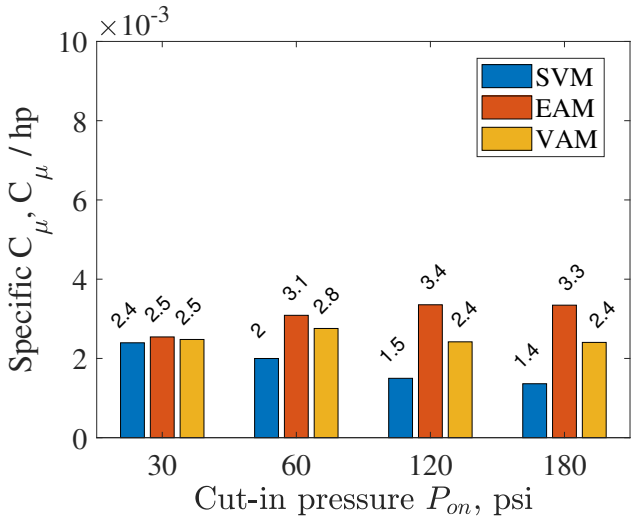


Figure 15: Specific Momentum Coefficient, $\overline{C_\mu}$

### 2.6.2 Slalom Maneuver

For the slalom maneuver, the roll input resulted in the output $C_\mu$ oscillating with an amplitude of 0.0245 or 49% of max $C_\mu$ as seen in figures II.16(a) and II.16(b). Referring to these figures, the slalom maneuver was conducted with no input from the compressor to replicate a compressor-failed condition. The results show that EAM valve metering allows for the longest sustained slalom, which is consistent with the max roll input results. The aircraft trajectory maintains the slalom until the AFC system is no longer able to produce the required momentum. The most significant differences in the compressor-off trajectories are due to the actuation time differences provided by configuration different valve meterings, EAM maintaining a slalom 4 times longer than SVM, and VAM achieving a slalom 3 times longer than SVM.

The configurations activate the compressor at differing points, and $CL_{[\text{-}]}$ indicates the slalom

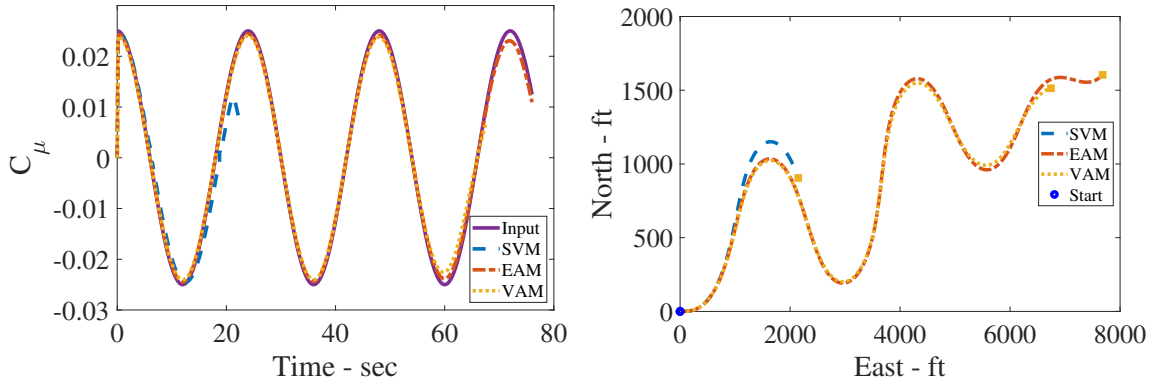


(a) Slalom Output $C_\mu$ (b) Aircraft trajectory

Figure 16: Compressor off operation

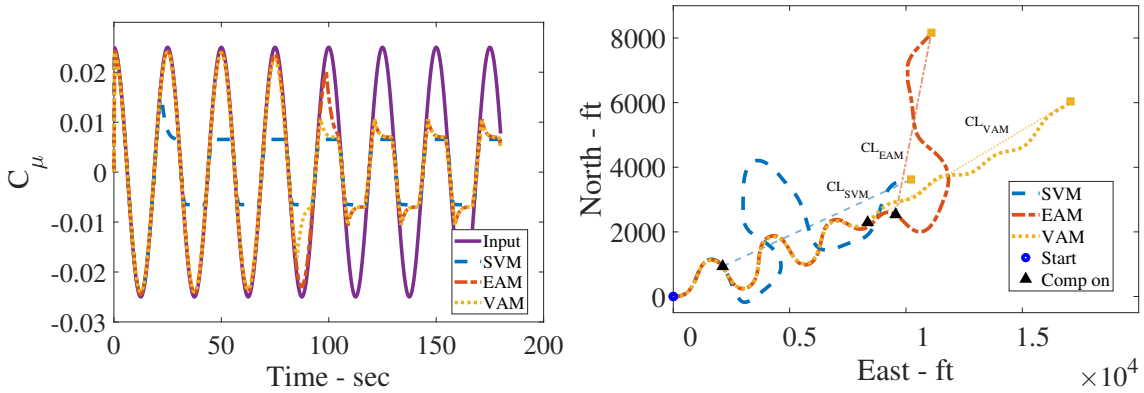


(a) Slalom Output $C_\mu$ (b) Aircraft trajectory

Figure 17: Performance with compressor and tank operational.

centerline during compressor operation.

The centerlines for the various meterings differ due to the slalom input amplitude reducing at different points along the original signal path, which can be seen in Fig. II.17(a) where SVM and VAM begin to decay at 0.015 $C_\mu$ and EAM at 0.02 $C_\mu$. In Fig. II.17(b), the SVM trajectory fails to achieve a slalom maneuver once the supply tank is depleted and switches the compressor on. EAM has an initialization transient for the first 40 seconds when the compressor turns on while VAM maintains nearly the same original trajectory when transitioning to the reduced amplitude slalom. These results show that the compressor is able to sustain a reduced-amplitude slalom maneuver after tank discharge. The compressor-only achievable amplitude corresponds to a $C_\mu$ output slightly under 0.0075, or 30% of the

originally commanded slalom input amplitude.

Figure II.18(a) shows the SVM configuration has the highest centerline drift by several orders of magnitude, with VAM outperforming EAM with the least centerline drift. The large drift error of the SVM configuration may be attributed to the SVM system's inability to periodically repressurize the plenum as the commanded $C_\mu$ approaches zero. The compressor in the EAM and VAM configurations can produce enough mass flow and have a small charging period when the commanded $C_\mu$ is below 0.01, which may be contributing to those configurations holding a more stable slalom than SVM once the compressor turns on. This behavior is probably attributed to the exit area controller in the EAM and VAM configurations, allowing the aircraft to compensate for the system's reduced mass flow output by altering the plenum exit area and thus allowing the compressor to overcome the system's exit mass flowrate. This phenomenon can be seen in Fig. II.18(b), where both the EAM and VAM meterings have the highest specific momentum coefficient. Although EAM has the highest specific $C_\mu$, the benefit of having higher $C_\mu$ generation efficiency does not directly translate to increased tracking performance for the slalom maneuver. Centerline drift indicates that a combination of both supply and exit area control is needed to keep the aircraft in a slalom. The specific momentum results show trends consistent with the max roll test, and indicate that the benefits of $C_\mu$ generation with EAM and VAM become increasingly clear with sustained compressor usage.

## 2.7 Overall Performance and Comparison

Comparing the three-valve meterings, one might assume that EAM provides the best performance. It provides the highest specific $C_\mu$, longest actuation time, a moderate rise time, and the largest total $C_\mu$ and power specific $C_\mu$. The flight performance results show that although EAM provides a longer actuation time, it underperforms during flight maneuvers whenever

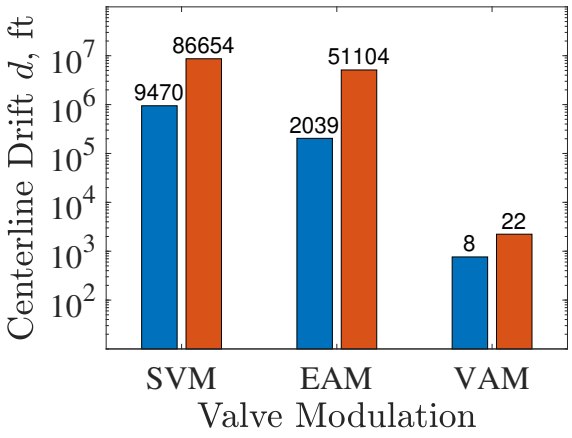


(a) Centerline drift

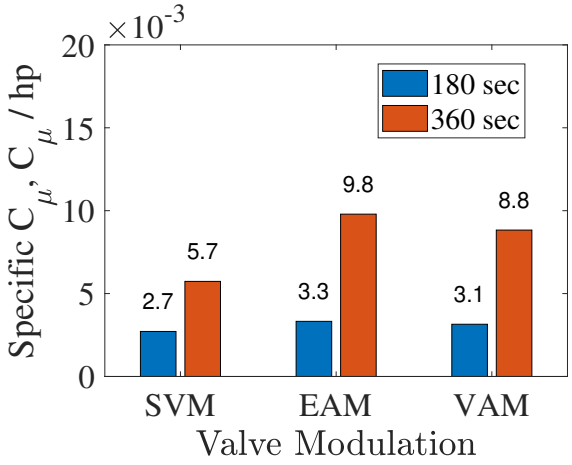


(b) Specific momentum coeff

Figure 18: Slalom centerline drift and specific momentum coefficient show the effect of the valve meterings on the maneuver.

the tank is depleted when compared to the VAM metering. Although the VAM metering has moderate actuation time and specific $C_\mu$, it provides the best overall flight performance in terms of slalom tracking.

While this study shows that VAM achieves the best overall performance, the approaches have differences in implementation complexity and structural requirements. Although the SVM metering has limited performance, it is comparatively simple to implement, requiring only a single actuated valve, and can be constructed with commercially-available components. The EAM and VAM systems are more complex as they require controllers to adjust the plenum

slot openings, which are custom parts and more involved.

EAM does not enforce plenum pressure limitations. Plenum pressure ratings are likely to achieve lower ratings than the supply tank (e.g., rapid prototyping fabrication of plenum examples for this aircraft with a working pressure of 30psi demonstrated ultimate failure at 45psi), and any fielded system will require a mechanism to limit pressure in the discharge components. SVM applied to enforce plenum pressure limits results in a VAM configuration.

# CHAPTER III

# SYSTEM IDENTIFICATION FRAMEWORK

## 3.1 Flow Field Modeling

### 3.1.1 Isolated rotational structure

The AZZ tornadic vortex structure encodes a minimal set of parameters of interest to forecasters: tornado size, wind speed, and location. The model assumes that a tornado, modeled as a vortex, has a certain core radius $R_{core}$, a max tangential velocity $V_{\theta,max}$, and is centered at $(x, y)$ in a two-dimensional plane, as illustrated in Fig. 19.

The radial velocity of the tornado is given by

$$v_\theta(r) = 2V_{\theta,max}\frac{r/R_{core}}{1 + (r/R_{core})^2}. \tag{3.1.1}$$

The radial distance $r$ from the center of the tornado is converted to Cartesian coordinates to define the location of the tornado in latitude, longitude like coordinates (The simulation implements it as North and East distances). For a tornado centered at $(x_0, y_0)$,

$$\Delta x = x - x_0, \quad \Delta y = y - y_0, \tag{3.1.2}$$

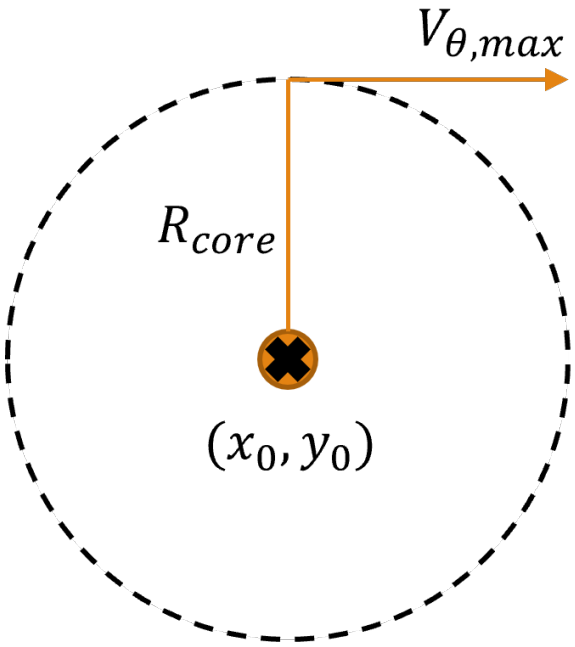

Figure 19: Minimal tornado vortex parameterization

and

$$r = \sqrt{(\Delta x)^2 + (\Delta y)^2}. \tag{3.1.3}$$

### 3.1.2 Flow velocity components

Although the definition of the flow field tangential velocity provides a compact description, it is not the quantity measured by a local measurement system, as happens when a multi-axial sensor or estimation scheme resolves the wind velocities at a certain position. For this, we use the definition of the tangential flow in a flow potential where

$$v_\theta = \frac{\Gamma}{2\pi r} \tag{3.1.4}$$

and the definition of the directional velocity components $u$ and $v$ as

$$u = \frac{\Gamma \Delta y}{2\pi r^2} \tag{3.1.5}$$

and

$$v = -\frac{\Gamma \Delta x}{2\pi r^2}. \tag{3.1.6}$$

Substituting equation 3.1.4 into equations 3.1.5, 3.1.6, the the wind velocity components in rectangular coordinates is

$$u = \frac{v_\theta \Delta y}{r} \tag{3.1.7}$$

$$v = -\frac{v_\theta \Delta x}{r} \tag{3.1.8}$$

### 3.1.3 Embedded tornado

The other flow field modeled is the AZZ vortex model embedded with a bulk uniform flow. The bulk uniform flow, shown in figure 20, is influenced by two parameters, the flow velocity $v_\beta$ and the flow direction $\beta$. The flow is embedded into the AZZ Cartesian flow direction coordinates $(u, v)$ to form the embedded flow velocities $u_{emb}$ and $v_{emb}$.

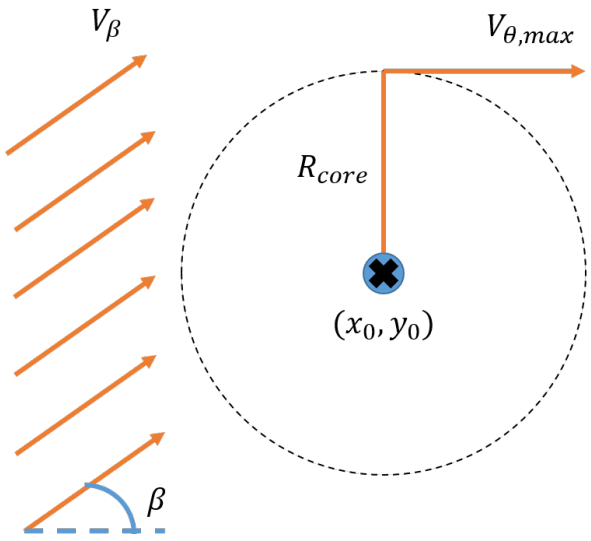


Figure 20: Embedded Flow Parameters

$$u_{emb} = u + V_\beta \cos\beta \tag{3.1.9}$$

$$v_{emb} = v + V_\beta \sin\beta \tag{3.1.10}$$

## 3.2 Gust response and flight dynamics simulation

The underlying flight dynamics model is a linearize flight dynamics framework [2], which incorporates exogenous disturbances to describe gust response [44, 45].

Data is collected using a spatio-temporal interpolation routine defined in [37] to provide estimates of the wind field. The routine implements 4D (3 spatial, 1 temporal degree of freedom) linear interpolation, where the change in a unit area is measured for different time instants, which can be evaluated as a 4D first order Taylor expansion that evaluates the unit area for the three wind velocity components $u, v, w$.

Incorporating the wind velocity measurements for the wind field into something related to the aircraft, the state space model used for the assumed aircraft incorporates gust disturbance in the form

$$\dot{x} = Ax + Bu + B_g g, \tag{3.2.1}$$

where $A$ and $B$ are the plant and control dynamic matrices, respectively, and $x$ and $u$ are the system and control states. The gust disturbance, $g$, is modeled with the directional velocity measured from the wind field

$$g = \begin{bmatrix} u \\ v \end{bmatrix}. \tag{3.2.2}$$

Since the purpose of the system identification is to identify the parameters of the tornado wind field, it is assumed that the aircraft state space model is known, with the matrix containing describing the gust influence $B_g$ assumed to be identity. With this assumption, it is assumed that the aircraft has perfect measurement of the wind field and there is no interference with the sensors onboard.

## 3.3 Parameter Estimation

Least squares regression was used to estimate the parameters in the tornado model. The regression method minimizes the error $\varepsilon$ between the estimate of the wind field wit the true wind field data collected by the UAS.

$$\varepsilon_n = \sum_{k=1}^{t_f} \left(\hat{g}_k - g_k\right)^2 \tag{3.3.1}$$

$$\hat{g} = f\left(\hat{\theta}\right) \tag{3.3.2}$$

$$\hat{\theta} = [V_{\theta,max}, R_{core}, x_0, y_0] \tag{3.3.3}$$

Once the least square error is calculated, the overall error across each UAS in the swarm is averaged. This averaged error is then minimized to acquire the best estimate for the tornado model.

$$V_N(\theta) = \frac{1}{N} \sum_{n=1}^{N} \varepsilon_n \tag{3.3.4}$$

$$\hat{\theta}_N = \textbf{arg min } V_N(\theta) \tag{3.3.5}$$

For this system, the inputs used the flight path for the UAS, which would be the inputs to the control surfaces if looking at the state space model in equation 3.2.1. The outputs are the directional wind velocities, $u$ and $v$.

## 3.4 Flight simulation

The aircraft flight simulation was implemented in MATLAB using the interpolation routine outlined in [37] with a 10 Hz frequency.

All simulation trials were benchmarked to a tornado in Mullinville, KS in 2002 which was estimated to have a core radius of 265 m and max tangential velocity of 34.8 m/s.

The embedded flow field has a bulk flow at 10 m/s with a direction at 20 degrees north of east.

### 3.4.1 Flight trajectories

Three trajectories were selected. Two single agent cases, and one multi-agent case.

In order to understand the importance of having multiple agents in the estimation process, trials were first conducted with one UAS to see if reasonable estimates were achievable.

The UAS flown in these trials used two different maneuvers. The first was a circular loiter around the tornado and the other was a slalom along one edge of the tornado. The better performing of the two trajectories was selected to be implemented into the multi-agent case.

For Both the single and multiple agent cases, the minimum distance to the center of the vortex was increased in increments of 500m to observe the effectiveness of each case with increased distance from the tornado. This is valuable part of the experiment as it will reveal under ideal conditions, the farthest a single UAS or swarm can be from a tornado and still translate relevant information about its structure.

**Circular loiter** For the circular loiter case, two scenarios were simulated. The first scenario focuses on the effect of the radius of the loiter. The flight path radius was varied with a constant center. The other scenario observes the affect of location, with the loiter radius being held constant and the orbit center shifted above the vortex center. (see figure 21 for example flight path).

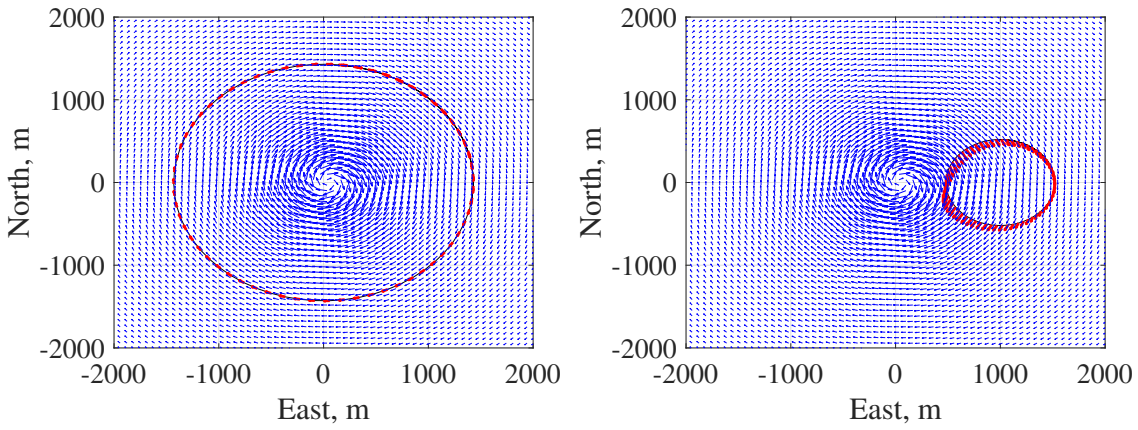


(a) Fixed Center (b) Fixed Loiter Radius

Figure 21: Estimator Errors

**Slalom (single agent)** The slalom trajectory was modeled as a sine function with a large enough amplitude,$a$, to be able to cross multiple contour lines as well as a sufficient period, $P$, to keep the slalom maneuver spaced out. The slalom is directed parallel to the vortex center to avoid the high speed and dynamic winds of the vortex center. (see figure 22 for example flight path)

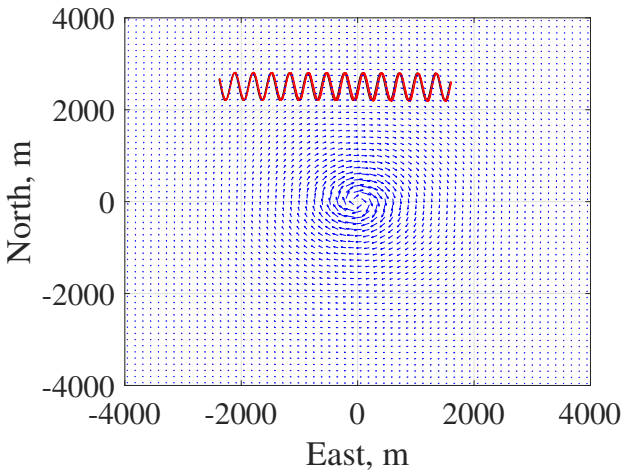


Figure 22: Slalom trajectory

$$y = a \sin\left(\frac{x(t)}{P}\right) \tag{3.4.1}$$

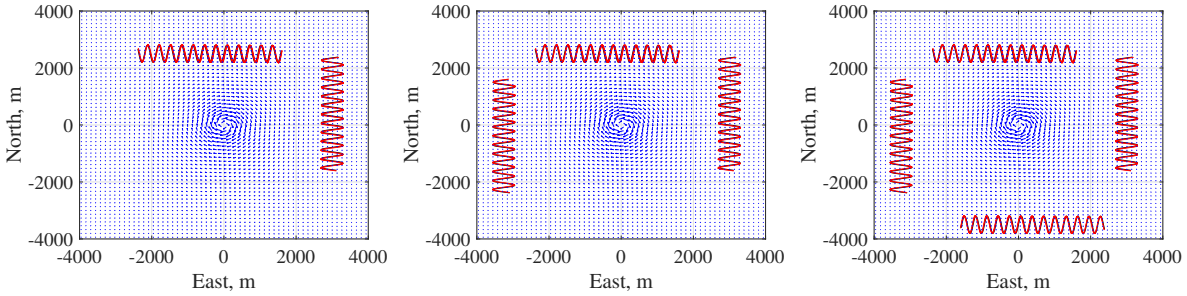


(a) 2 Agent (b) 3 Agent (c) 4 Agent

Figure 23: Multi-agent trajectories

**Multi-Slalom (multi-agent)** For the multi-agent analysis, multiple UAS are commanded in slalom maneuvers at different paths about the tornado to try and gather as much information on the different contours as possible. The paths were designed to be on different sides so that more contours can be observed by the swarm. The initial paths selected were chosen to be perpendicular to one another and as parallel as possible to the tornado so that the swarm can hit multiple contours while also keeping a safe distance from the tornado vortex. The simulator tested a combination of 2, 4, and 4 agents within the wind field (see Fig. 23 for a representation of the trajectories)

## 3.5 Simulation results

### 3.5.1 Single Agent Case

When observing the single agent cases, it is seen in Fig. 24 that they all share a similar pattern where after approximately 2.5 km, there is a sharp increase in the estimator error. It can be assumed that for an ideal case, the farthest an aircraft should fly from the vortex core should be no more than 2 km. Within this region, a single aircraft can acquire estimates with less than 1% error.

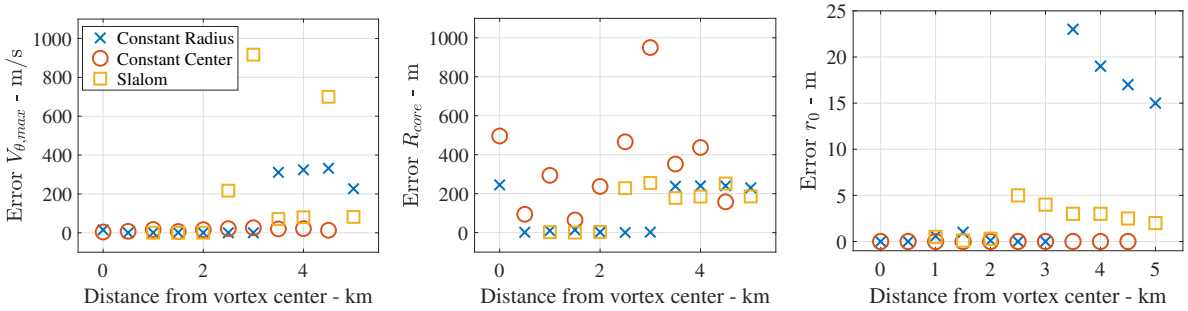


(a) $V_{\theta,max}$ Error (b) $R_{core}$ Error (c) Relative radius Error

Figure 24: Estimator Errors

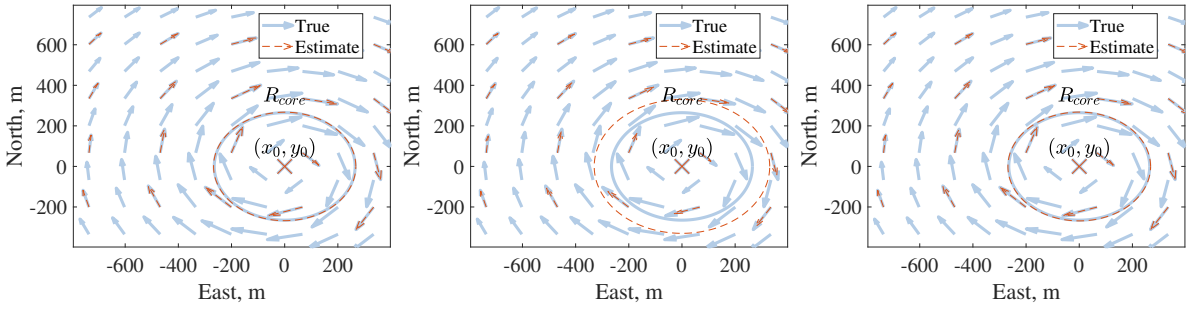


(a) Fixed Radius (b) Fixed Center (c) Slalom

Figure 25: Wind Field Comparison for 2 km

Looking at figures 25 and 26, the deviation can be seen much more clearly, with the estimated tornado core radius and max tangential velocity changing drastically. The fixed radius may seem to be more effective, however the increased range accuracy is due to the aircraft orbiting back within 2500 km of the vortex.

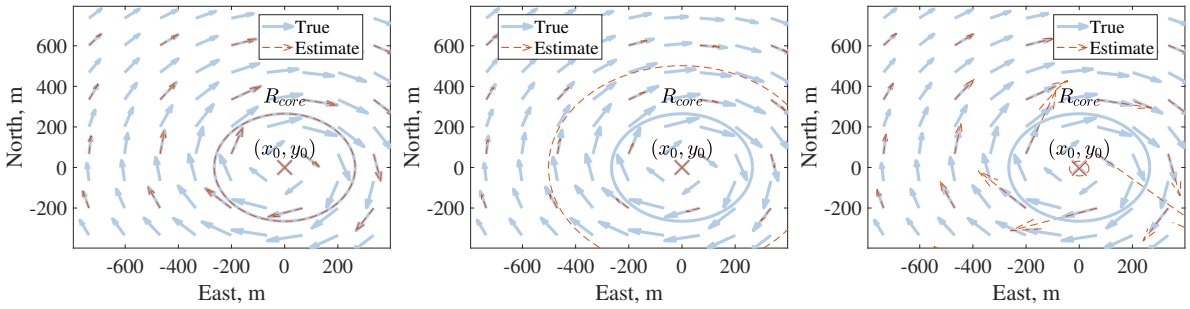


(a) Fixed Radius (b) Fixed Center (c) Slalom

Figure 26: Wind Field Comparison for 2.5 km

The slalom maneuver provides the most consistent estimates for the tangential velocity and core radius estimates and has an acceptable ±5m difference with the relative location of the tornado. These are the reasons why it was selected as the flight path for the multi-agent swarm. Additionally, the slalom flight path is able to more freely cross over more contour lines, which provides more data on the field and thus a better estimate of the tornado parameters.

### 3.5.2 Multi-Agent Analysis

For the multi-agent analysis, the UAS are given inputs of slalom maneuvers at various path about the tornado to try and gather as much information on the different contours as possible. Here, we will observe if the estimate quality is improved for the system. Here, we compare the estimate quality of 1, 2, 3 and 4 agents in the swarm at various orientations about the tornado (see Fig. 27).

Looking at the errors and the reconstructed wind fields in figures 28 and 29, there is a clear benefit to implementing multiple agents into a vortex wind field. There is a considerable increase in accuracy/ reduction in error past the 2.5 km mark and even continues to provide quality estimates up to 5 km away from the cortex center. This can be attributed to the fact since there are more agents in wind field, that are at staggered distances from the vortex, more contour lines are crossed and thus more data to build up an estimate of the tornado

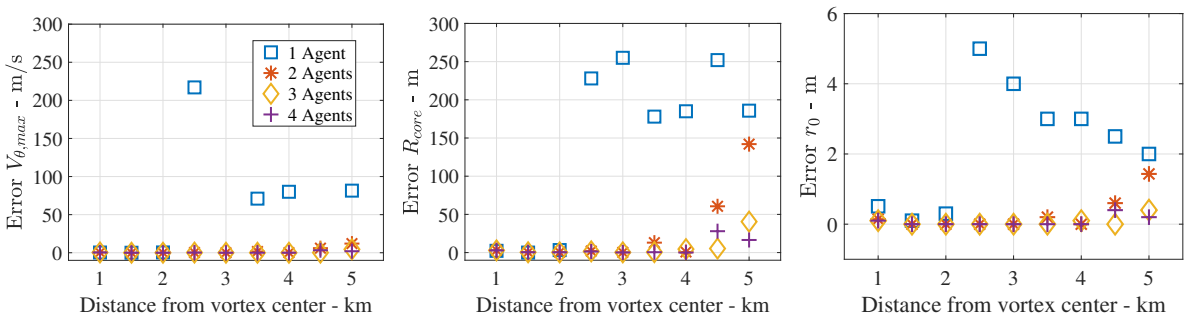


(a) $V_{\theta,max}$ Error (b) $R_{core}$ Error (c) Relative radius Error

Figure 27: Multiple Agent Estimator Errors

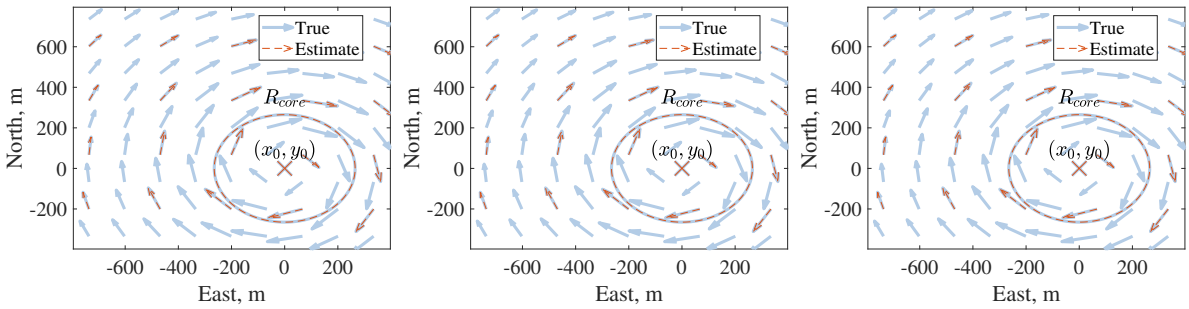


(a) 2 Agents (b) 3 Agents (c) 4 Agents

Figure 28: Multiple Agent Wind Field Comparison for 2 km

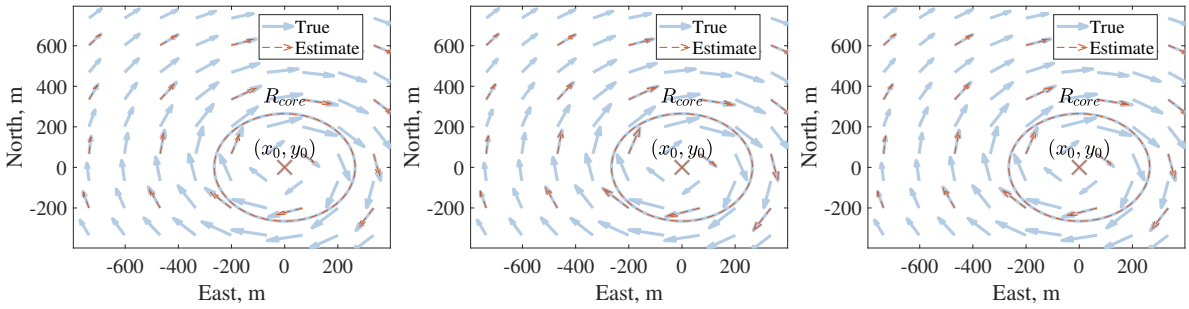


(a) 2 Agents (b) 3 Agents (c) 4 Agents

Figure 29: Multiple Agent Wind Field Comparison for 2.5 km

parameters.

# CHAPTER IV

# INFORMATION OPTIMIZING FLIGHT PATHS FRAMEWORK

## 4.1 Parameter Interchange Estimation

From [30], the flow field identification accuracy deteriorated as the aircraft flew farther from the vortex source (more than 6 times the true parameter values of $V_{max}$ and $R_{core}$ at distances above 2 km from the vortex center). To understand the reason for this deterioration, the error for a range of possible combinations of both parameters (0 - 300 m/s, m for $V_{max}$ and $R_{core}$ respectively) is plotted and observed in figure 30. Performing this procedure, it is observed that the resulting error local minima increase as the identification is performed at increased distances from the vortex center. What is also interesting from this study is that the local minima follow a somewhat symmetrical arc that falls on the interchanged values of the parameter estimates of $V_{max}$ and $R_{core}$.

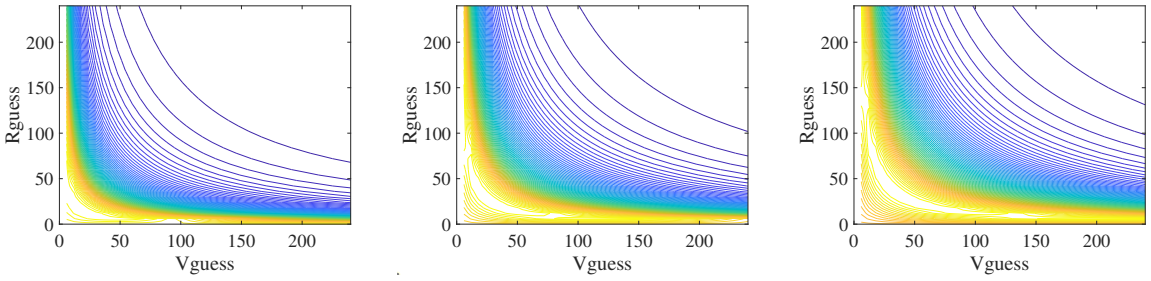


(a) 1km (b) 2km (c) 3km

Figure 30: Error contours of parameter combinations at varying distances from vortex center

With this characteristic, a flight trajectory to identify the vortex parameters can be guided by this phenomenon. This trajectory entails comparing the $V_{max}$ and $R_{core}$ parameter estimates with the interchanged estimate and calculate the resulting error. The aircraft seeks locations in the flow field that maximize this error in order to find the $V_{max}$ and $R_{core}$ parameter estimate global minimum. The aircraft performs an estimate, then compares this estimate with the interchanged values, and calculates the resulting error. If the error is below a certain threshold, the aircraft moves closer to the estimated center. Once the error increases to a certain threshold, the parameter estimate can be considered reliable. This process is highlighted in figure 31.

$$\hat{\theta} = [V_{\theta,max}, R_{core}, x_0, y_0] \tag{4.1.1}$$

$$\hat{\theta}_{inverted} = [R_{core}, V_{\theta,max}, x_0, y_0] \tag{4.1.2}$$

$$\varepsilon_{inverted} = |\hat{\theta} - \hat{\theta}_{inverted}| \tag{4.1.3}$$

## 4.2 Information Optimization

Contemporary flow field parameter estimation approaches generally include an approach rather than a flow field dependent. In [30], aircraft flight paths were specified a priori and their performance evaluated. The parameter interchange technique leaves open the choice of acceptable error threshold, which may or may not be achievable given current measurement conditions.

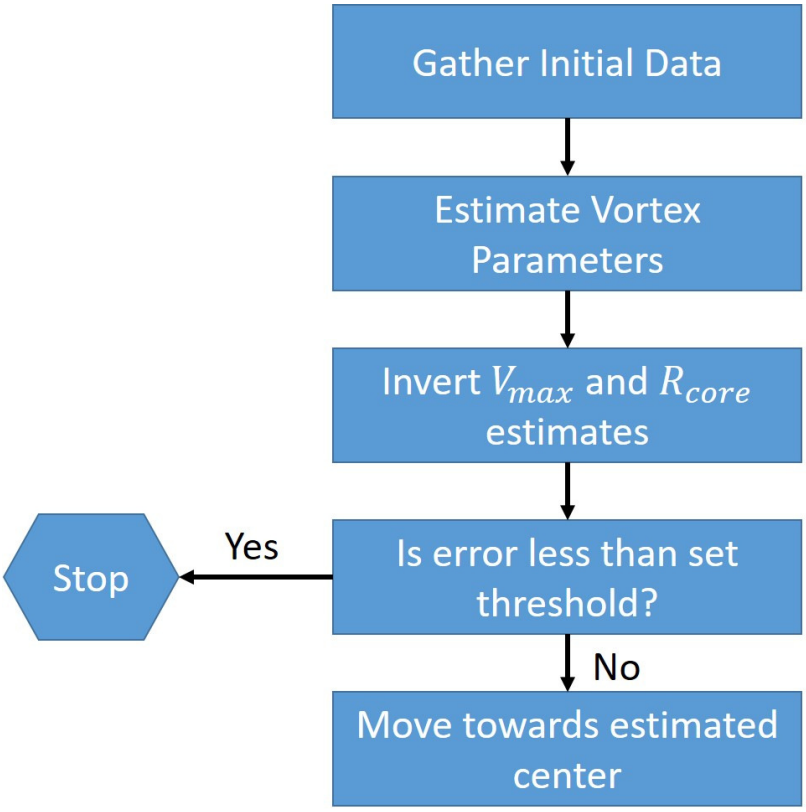


Figure 31: Inverted Estimation Process

An alternative approach is to provide parameter error minimization through information maximization, reducing the reliance on user-specified conditions and allowing generalization to other flow field structures. This method would also reveal the best (in a flow structure estimation context) possible path to follow in a flow field. Such an approach first requires a systematic definition of 'information' in the context of wind field measurement. This information term should consist of parameters that affect the parameter estimate quality, such as flight path distance, data density, average spatial gradient, and gradient variance.

### 4.2.1 Wind structure information definition

The flight path length $p$ was selected to encode the intuition that as the aircraft covers more distance, the aircraft collects more data and hence more information on the flow structure.

Information recovery is also proportional to the flow field structure's spatial gradient, defined as the rate of change of the flow velocity over the change of the flow field structure parameter. For instance, one of the spatial derivatives is the rate of change of the flow velocity over the change of the flow structure with respect to max tangential velocity $V_{max}$.

$$\frac{1}{p}\int \frac{\partial v_\theta}{\partial \theta} dp \tag{4.2.1}$$

The spatial gradient forms the core of the information term as different flow structures will have different spatial gradients. Areas where the spatial gradient is largest are areas where the different flow structures are more distinguishable, and data gathered from these areas is most valuable to extracting accurate estimates. The spatial gradient average observed by the aircraft is used to influence its motion towards areas where the spatial gradient is largest.

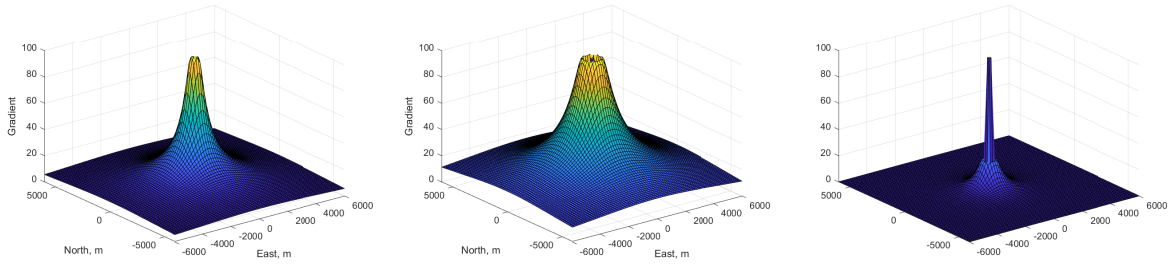


(a) $V_{max}$ (b) $R_{core}$ (c) $r$

Figure 32: Gradient Fields

The gradient variance $\sigma$ is included to quantify the idea that trajectories with more contour crossings improve the flow structure estimate accuracy. Data density $\rho$ is used to quantify the effect of aircraft measurement sparsity and its detrimental effect on estimate uncertainties.

The information term is then normalized by the maximum gradient experienced for each of the flow field parameters. This normalization was implemented using two different methods: global maximum and relative maximum. The global maximum gradient is defined as the max

total gradient *expected* across the entire estimated flow field, with gradient fields shown in figure 32. The relative maximum gradient is defined as the max gradient *observed* by the aircraft over its trajectory, as shown in figure 33.

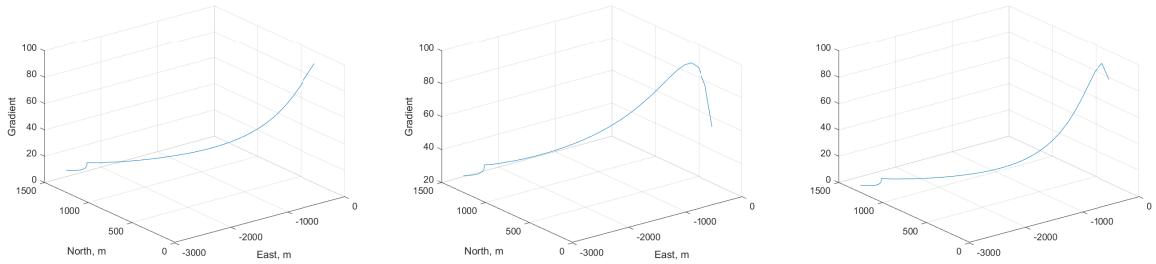


(a) $V_{max}$ (b) $R_{core}$ (c) $r$

Figure 33: Relative Aircraft Gradients

The information term $I_\theta$ for a parameter $\theta$ may then be summarized as

$$I_\theta = p\sigma\frac{\rho}{p}/\max\left(\frac{\partial v_\theta}{\partial\theta}\right)\int\frac{\partial v_\theta}{\partial\theta}dp, \tag{4.2.2}$$

which is simplified to

$$I_\theta = \sigma\rho/\max\left(\frac{\partial v_\theta}{\partial\theta}\right)\int\frac{\partial v_\theta}{\partial\theta}dp. \tag{4.2.3}$$

The total information is the sum of the information terms for $N$ parameters (ie for the isolated structure, it is a sum over the $V_{max}, R_{core}$, and $r$ information terms).

$$I = \Sigma_{n=1}^{N} I_{\theta,n}. \tag{4.2.4}$$

### 4.2.2 Minimization Technique

A dynamic modeling approach was used in order to optimize the information gathered by the aircraft. The aircraft minimizes the entropy $E = I^{-1}$ (information inverse) to identify the location with the highest expected information. The minimization routine is implemented in

two ways: as a function of the aircraft location $E(x, y)$, and as a function of aircraft heading $E(\Delta\psi)$. The distance constraint is implemented such that the aircraft is constrained to move at a constant velocity. The optimization was then implemented via dynamic programming as

$$\begin{aligned} &\min E(x, y) \\ &\text{s.t.} \quad \Delta d = \sqrt{\Delta x^2 + \Delta y^2}. \end{aligned}$$

The second case added a heading constraint to the optimization to provide an achievable waypoint for the aircraft to fly towards.

$$\min E(\Delta\psi) \tag{4.2.5}$$

$$\text{s.t.} \quad \Delta d = \sqrt{\Delta x^2 + \Delta y^2} \tag{4.2.6}$$

$$\Delta\psi_{max} \geq \Delta\psi \tag{4.2.7}$$

## 4.3 Flight path results

### 4.3.1 Inverted Estimation

Implementing the inverted estimation method, the aircraft was able to successfully estimate the vortex parameters within 10% of the true values. Depicted in figure 34, the aircraft flies directly towards the center of the vortex until the acceptable threshold is met. For this example, the threshold was determined as 3 orders of magnitude (100). This criterion led the aircraft to stop two times the core radius away from the vortex center.

The figure depicts the simulated true flow field (blue) as well as the estimated flow velocities

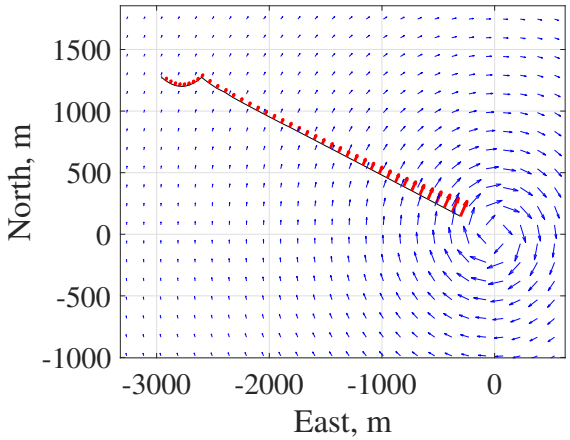

Figure 34: Isolated vortex Inverted Estimation Information Path

from the aircraft (red). Although this method recovered parameter estimates, it is limited by the need to determine the acceptable error value at which to terminate search as well as relying on the assumption that the aircraft can reliably locate the vortex center. Additionally, this method does not clearly identify where the best information is located in the flow field.

### 4.3.2 Optimized Information Paths

**Relative Maximum** From the single-constrained case simulation results in figure 35, the aircraft travels approximately 700 m towards the center of the vortex and then alternates directions on a line segment perpendicular to the flow velocity.

This flight path provides an average parameter estimate, with errors more than 30% of the true values. When looking at the embedded flow structure, the aircraft flies through the center of the field. This suggests that as flow structures become more complex, the path with the most information may be the one that takes the aircraft toward the major source or sink of the flow.

When the heading constraint is added, the estimated error drops below 2% of the true values

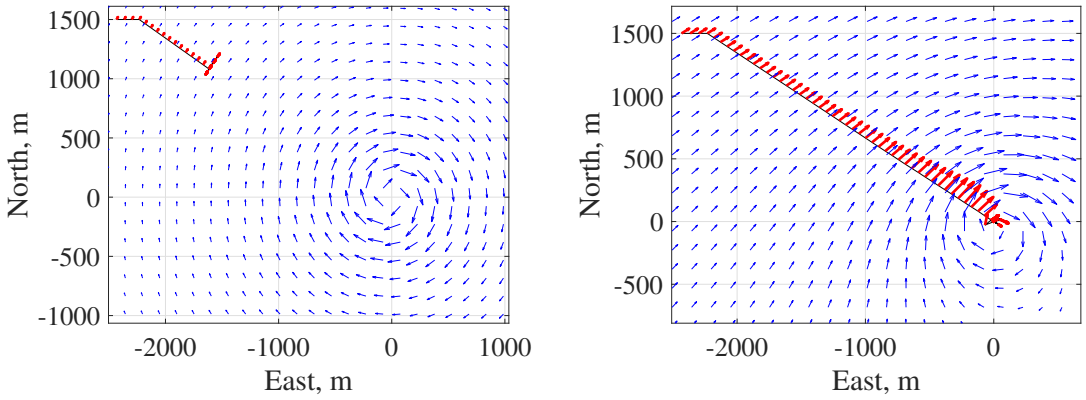


(a) Isolated vortex (b) Embedded Flow

Figure 35: Relative Max Information Paths with distance constraint

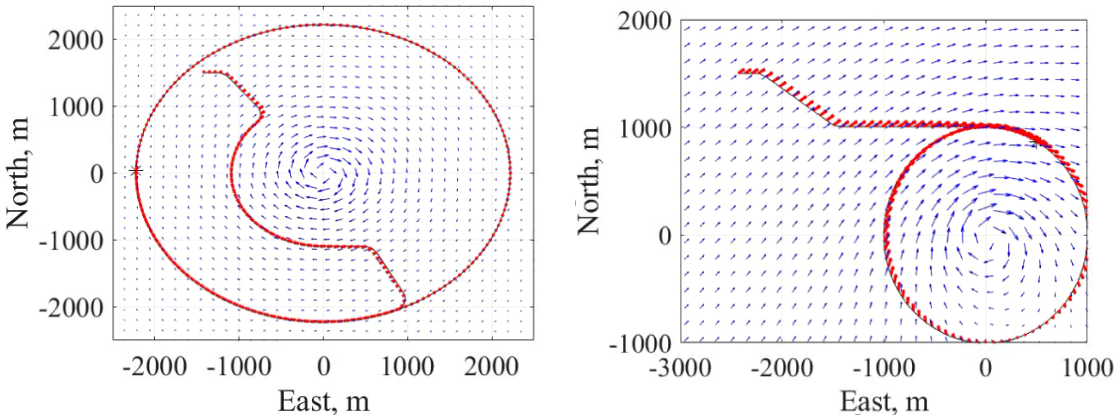


(a) Isolated vortex (b) Embedded Flow

Figure 36: Relative Max Information Paths with distance and heading constraint

for both flow structures. It seems the heading constraint smoothes out the aircraft's flight path and provides a much smoother path. Additionally, it seems the heading constraint paired with the relative max spatial derivative information term leads the aircraft to follow the region close to the peak of the $R_{core}$ gradient field. This may be due to the fact that the $R_{core}$ gradient field peaks at a larger radius than the other parameters.

**Global Maximum** The simulation results in figure 37 show that the path with the most information is one that travels into the vortex center and keeps looping and passing through the center of the vortex. This flight path provides a lower estimate error in the single

constrained case (less than 10%). When the heading constraint is added (see figure 38), the aircraft still flies toward the center and spends the majority of the flight gathering data, but now it loops and passes through the center of the vortex. This method provides a lower estimate error less than 5% of the true values.

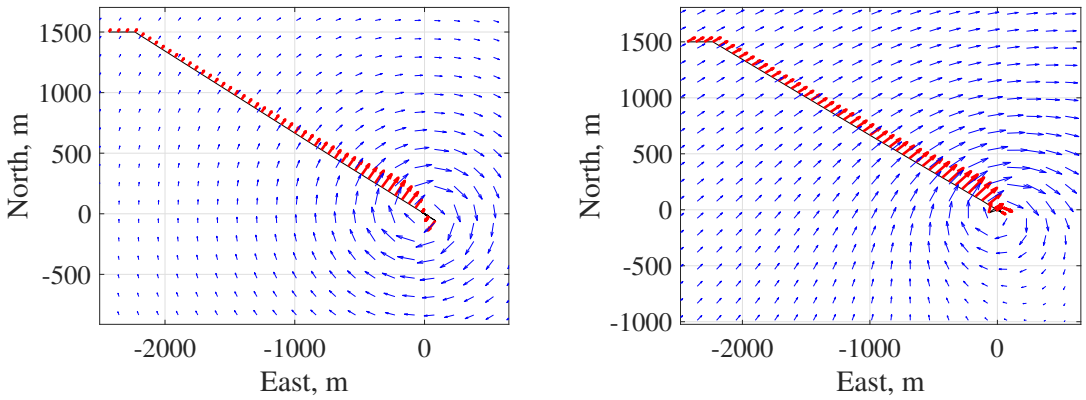


(a) Isolated vortex (b) Embedded Flow

Figure 37: Global Max Information Path

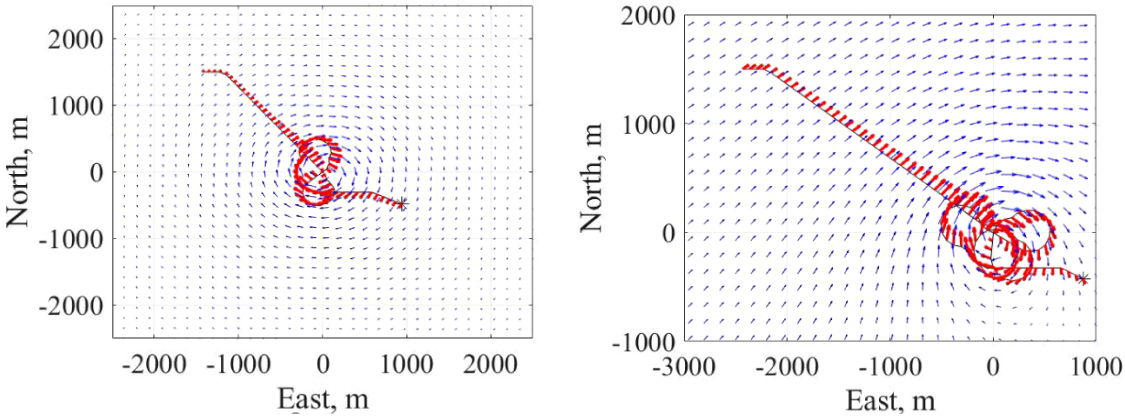


(a) Isolated vortex (b) Embedded Flow

Figure 38: Global Max Information Paths with distance and heading constraint

What seems to be common from the methods discussed is that including the heading constraint improves the estimate error greatly, with some cases decreasing by 5%. The inclusion of the heading constraint may help the optimizer from getting stuck at one point and forces the aircraft to "explore" the flow field. This addition also prevents the aircraft from following a sporadic path and allows for more achievable flight paths.

# CHAPTER V

# CONCLUSION

Comparing the three-valve meterings, the supply control provides the lowest actuation time and specific $C_\mu$, meaning it is the least efficient in managing the available air within the system. Exit area control gives the best performance in terms of actuation time and $C_\mu$ generation, and when both strategies are combined for VAM, the benefits from EAM are more dominant than the negative performance from SVM.

Simulated flight performance results show that using a supply-based control results in the highest trajectory error, and underperforming system metrics for dynamic maneuvers such as a slalom. The exit area control strategy has the best system transient response, longest actuation, and most efficient power requirements. These results do not translate to flight tracking transients when exit area control is exclusively used. Although implementing both supply and exit area control strategies performs at lower system performance than exclusive exit area control, this distributed control approach significantly outperforms the other methods when the supply tank is exhausted.

This paper shows that there are improvements to the AFC system's transient response, run time, and power requirements whenever a form of exit area control is implemented. Additionally, it is shown that there are increased improvements to flight path tracking when the VAM metering, a form of both supply and exit area control, is implemented at the cost of

increased system architecture complexity due to incorporating two uncoupled feedback loops.

This paper also shows the feasibility of piston-based compressors supplying auxiliary mass-flow can improve a system's run time when used at certain supply tank pressures. The paper shows that the compressor provides the best specific $C_\mu$ or most efficient $C_\mu$ generation when used around the compressor's ideal pressure ratio.

Additionally, the paper demonstrates that the compressor can provide enough mass flow to the system when the tank is depleted to sustain minor maneuvers such as gust correction or a shallow slalom, showing that the aircraft can still maneuver for periods longer than what the supply tank can support.

The results open the path to implementing relatively cheap commercial off-the-shelf piston compressors onto UAS with AFC systems. Designers can now be more informed on system design choices when implementing such systems, reducing the total cost of realizing such a system.

The information framework study has shown that a flight path influenced by the flow field gradients is achievable through simulation and can provide reliable parameter estimates using an MSE framework of different flow fields. These flight paths reduce the need to specify an achievable accuracy or the UAS flight paths, in favor of providing an initial field model to compare with the true flow.

Simulations of the three methods indicate that the flight path incorporating an information term defined by the relative maximum flow gradients and including both distance and heading constraints provides the most accurate flow measurements. Relative to the other methods considered, this approach reduced parameter estimation error by at least a factor of 5.

## 5.1 Future Work

With the study of the AFC system and the development of the information path framework, it is shown that the AFC aircraft can determine flow structures from gathered wind data. Since the study was possible with a simplified flow field structure source, future work would include using more complex flow structures that may represent some object of interest causing a large disturbance in the flow field. An example of this would be tracking a large ship at sea with limited onboard radio capabilities and seeing if the aircraft can locate the ship.

Future work from this paper also includes implementing the information optimization routine to model 3D flow fields utilizing multiple aircraft. Work on determining a data fusion strategy between the multiple agents is currently being pursued.

## REFERENCES


[1] *Active Flow Control Concepts on a Highly Loaded Subsonic Compressor Cascade: Résumé of Experimental and Numerical Results*, Turbo Expo: Power for Land, Sea, and Air, vol. Volume 7: Turbomachinery, Parts A, B, and C, 06 2011.

[2] *Modeling and simulation of miniature aerial vehicles*, ch. 8, pp. 623–663, John Wiley & Sons, Ltd, 2015.

[3] Robert L. Ash, Irfan Zardadkhan, and Allan J. Zuckerwar, *The influence of pressure relaxation on the structure of an axial vortex*, Physics of Fluids **23** (2011), no. 7, 073101.

[4] Robert L. Ash and Irfan R. Zardadkhan, *Non-equilibrium behavior of large-scale axial vortex cores*, AIP Advances **11** (2021), no. 2, 025320.

[5] Kuan Thai Aw and Kim Tiow Ooi, *A review on sliding vane and rolling piston compressors*, Machines **9** (2021), no. 6, 125.

[6] Randal W Beard and Timothy W McLain, *Small unmanned aircraft*, Princeton university press, Princeton, NJ, 2012.

[7] Jennifer L. Cardona, Katherine L. Bouman, and John O. Dabiri, *Wind speed inference from environmental flow–structure interactions*, Flow **1** (2021), E4.

[8] Christian Coletti and Imraan A. Faruque, *Flight dynamics integration approach for aircraft using active flow control as primary control surfaces*, AIAA SCITECH 2022 Forum, 2022.

[9] Crane Technical Publications Unit, *Flow of fluids through valves, fittings, and pipes*, (1980), no. 410.

[10] W J Crowther and L T Gomes, *An evaluation of the mass and power scaling of synthetic jet actuator flow control technology for civil transport aircraft applications*, Proceedings of the Institution of Mechanical Engineers, Part I: Journal of Systems and Control Engineering **222** (2008), no. 5, 357–372.

[11] Kaiyang Ding, Junfeng Yang, Hui Lin, Zhao Wang, Deyi Wang, Xiaohao Wang, Kai Ni, and Qian Zhou, *Towards real-time detection of ships and wakes with lightweight deep learning model in gaofen-3 sar images*, Remote Sensing of Environment **284** (2023), 113345.

[12] Olivier Dumont, Antoine Parthoens, Rémi Dickes, and Vincent Lemort, *Experimental investigation and optimal performance assessment of four volumetric expanders (scroll, screw, piston and roots) tested in a small-scale organic rankine cycle system*, Energy **165** (2018), 1119–1127.

[13] Rafael C Engel and Cesar J Deschamps, *Comparative analysis between the performances of reciprocating and rolling piston compressors applied to a domestic heat pump water heater*, International Journal of Refrigeration **102** (2019), 130–141.

[14] Alison B. Evans and Dryden Flight Research Facility., *The effect of compressor seventh-stage bleed air extraction on performance of the f100-pw-220 afterburning turbofan engine*, National Aeronautics and Space Administration, Ames Research Center, Dryden Flight Research Facility Edwards, Calif, 1991 (English).

[15] Longlong Gao, Gang Yang, Weijia Li, and Baoren Li, *Measurement of mass flow rate and evaluation of heat transfer coefficient for high-pressure pneumatic components during charge and discharge processes*, Flow Measurement and Instrumentation **45** (2015), 391–403.

[16] Constantions Georgiadis, *Modelling boat wake loading on long floating structures*, Computers Structures **18** (1984), no. 4, 575–581.

[17] David Greenblatt and Israel J. Wygnanski, *The control of flow separation by periodic excitation*, Progress in Aerospace Sciences **36** (2000), no. 7, 487–545.

[18] Christian Griffith and Imraan A. Faruque, *Modeling and system identification of pneumatic dynamics for active flow control systems on unmanned aerial vehicles*, Journal of Guidance, Control, and Dynamics (Awaiting government public release).

[19] ———, *System identification of pneumatic dynamics for active flow control aircraft*, AIAA Guidance, Navigation, and Control Conference at Scitech Forum 2023 (National Harbor, MD), AIAA, Awaiting government release.

[20] Rodney A. Hemmerly, *An investigation of the performance of a j52-p-8a engine operating under the influence of high bleed flow extraction rates.*, 1977.

[21] M. Jabbal, S. C. Liddle, and W. J. Crowther, *Active flow control systems architectures for civil transport aircraft*, Journal of Aircraft **47** (2010), no. 6, 1966–1981.

[22] T Kato, Y Shirafuji, and S Kawaguchi, *Comparison of compressor efficiency between rotary and scroll type with alternative refrigerants for r22*, (1996).

[23] Rudibert King, Notger Heinz, Matthias Bauer, Thomas Grund, and Wolfgang Nitsche, *Flight and wind-tunnel tests of closed-loop active flow control*, Journal of Aircraft **50** (2013), no. 5, 1605–1614.

[24] Linda Kral, *Active flow control technology*, ASME FED, Technical Brief (2000).

[25] John Lienhard IV and John Lienhard V (eds.), *A heat transfer textbook, 5th edition*, pp. 65–70,76, Phlogiston Press, Cambridge, MA, 2020.

[26] John C. Lin, Edward A. Whalen, Marlyn Y. Andino, Emilio C. Graff, Douglas S. Lacy, Anthony E. Washburn, Morteza Gharib, and Israel J. Wygnanski, *Full-scale testing of active flow control applied to a vertical tail*, Journal of Aircraft **56** (2019), no. 4, 1376–1386.

[27] Zhen Liu, Zheng Li, Dongsheng Xie, and Huawei Wu, *Unsteady characteristic and flow mechanism of a scroll compressor in small-scale compressed air energy storage system*, Journal of Energy Storage **51** (2022), 104368.

[28] Lennart Ljung, *Convergence and consistency*, ch. 8, pp. 251 – 252, Prentice Hall PTR, USA, 1999.

[29] E.H. Machu, *Survey of factors influencing reciprocating compressor efficiencies and discharge gas temperatures*, pp. 375–384, 12 2013.

[30] Abdalrahman Mansy and Imraan Faruque, *Tornado localization and structure identification from uav wind measurements*, AIAA Guidance, Navigation and Control Conference at SciTech 2023 Forum, Jan 2023.

[31] G. Maxwell and P. Rivera, *Dynamic simulation of compressed air systems*, 2003.

[32] Sangkyung Na, Myeongsu Shin, Gyungmin Choi, and Byungchae Min, *Effect of pressure ratio and oil viscosity on rotary compressor efficiency*, Journal of Mechanical Science and Technology **32** (2018), no. 10, 4971–4981.

[33] Robert C Nelson, *Flight stability and automatic control*, McGraw Hill, Boston, MA, 1998.

[34] Oasis Manufacturing, 23011 Alcalde, Laguba Hills, CA, *Xd4000-24 product specification*, xd4000-24 ed., 01 2009.

[35] AG Olabi, Tabbi Wilberforce, Mohamad Ramadan, Mohammad Ali Abdelkareem, and Abdul Hai Alami, *Compressed air energy storage systems: Components and operating parameters–a review*, Journal of Energy Storage **34** (2021), 102000.

[36] William J. Palm III (ed.), *System dynamics, 3rd edition*, pp. 431–440, McGraw-Hill, New York, NY, 2014.

[37] Ujjval Patel and Imraan Faruque, *Error characteristics of onboard wind field estimation via direct method in a simplified tornado model*, AIAA Guidance, Navigation and Control Conference at SciTech 2022 Forum, Jan 2022.

[38] Jan Petrich, Craig A. Woolsey, and Daniel J. Stilwell, *Planar flow model identification for improved navigation of small auvs*, Ocean Engineering **36** (2009), no. 1, 119–131, Autonomous Underwater Vehicles.

[39] Vijaykumar F Pipalia, Dipesh D Shukla, and Niraj C Mehta, *Investigation on reciprocating air compressor-a review*, International journal of Recent scientific research **6** (2015), no. 12, 7735–7739.

[40] Bjarne Dindler Rasmussen and Arne Jakobsen, *Review of compressor models and performance characterizing variables*, 2000.

[41] Nicholas Rathay, Matthew Boucher, Michael Amitay, and Edward Whalen, *Parametric study of synthetic-jet-based control for performance enhancement of a vertical tail*, AIAA Journal **52** (2014), no. 11, 2440–2454.

[42] Nicholas W. Rathay, Matthew J. Boucher, Michael Amitay, and Edward Whalen, *Performance enhancement of a vertical tail using synthetic jet actuators*, AIAA Journal **52** (2014), no. 4, 810–820.

[43] C. Rowley, D. Williams, T. Colonius, R. Murray, D. MacMartin, and D. Fabris, *Model-based control of cavity oscillations. ii - system identification and analysis*, 40th AIAA Aerospace Sciences Meeting & Exhibit, 2002.

[44] Utsav Saxena, Michael R. Dorothy, and Imraan A. Faruque, *Gramian-aware control approach for atmospheric gust harvesting*, Journal of Aerospace Information Systems **19** (2022), no. 1, 53–61.

[45] Utsav Saxena and Imraan A. Faruque, *Theoretical model for the gust performance of closed-loop flight control*, Journal of Guidance, Control, and Dynamics **40** (2017), no. 11, 2971–2975.

[46] Jonas Schröter, Tobias Graf, Daniel Frank, Christiane Bauer, Josef Kallo, and Caroline Willich, *Influence of pressure losses on compressor performance in a pressurized fuel cell air supply system for airplane applications*, International Journal of Hydrogen Energy **46** (2021), no. 40, 21151–21159.

[47] S. Scott Collis, Ronald D. Joslin, Avi Seifert, and Vassilis Theofilis, *Issues in active flow control: theory, control, simulation, and experiment*, Progress in Aerospace Sciences **40** (2004), no. 4, 237–289.

[48] R. Sebastián and J. Quesada, *Distributed control system for frequency control in a isolated wind system*, Renewable Energy **31** (2006), no. 3, 285–305.

[49] A. Seifert, A. Darabi, and I. Wyganski, *Delay of airfoil stall by periodic excitation*, Journal of Aircraft **33** (1996), no. 4, 691–698.

[50] Zhiwei Shi, Jiachen Zhu, Xinxi Dai, Kun Chen, Tongren Zhang, Haiyang Wang, Junquan Fu, Weimin Cai, and Peiliang Zhang, *Aerodynamic characteristics and flight testing of a uav without control surfaces based on circulation control*, Journal of Aerospace Engineering **32** (2019), no. 1, 04018134.

[51] Yong Liang Teh and Kim Tiow Ooi, *Theoretical study of a novel refrigeration compressor-part iii: Leakage loss of the revolving vane (rv) compressor and a comparison with that of the rolling piston type*, international journal of refrigeration **32** (2009), no. 5, 945–952.

[52] Fernando M Tello-Oquendo, Emilio Navarro-Peris, and José Gonzálvez-Maciá, *Comparison of the performance of a vapor-injection scroll compressor and a two-stage scroll compressor working with high pressure ratios*, Applied Thermal Engineering **160** (2019), 114023.

[53] Jonna Tiainen, Aki Grönman, Ahti Jaatinen-Värri, and Jari Backman, *Flow control methods and their applicability in low-reynolds-number centrifugal compressors—a review*, International Journal of Turbomachinery, Propulsion and Power **3** (2018), no. 1.

[54] Jijin Wang, Dehu Qv, Long Ni, and Yang Yao, *Experimental study on an injection-assisted air source heat pump with a novel two-stage variable-speed scroll compressor*, Applied Thermal Engineering **176** (2020), 115415.

[55] Clyde Warsop and William J. Crowther, *Fluidic flow control effectors for flight control*, AIAA Journal **56** (2018), no. 10, 3808–3824.

VITA

Abdalrahman Khaled Mansy

Candidate for the Degree of

Master of Science

Thesis: INFORMATION AWARE FLIGHT PATH DESIGN FOR
FLOW FIELD ESTIMATION AND
PERFORMANCE INVESTIGATION OF
ACTIVE FLOW CONTROL AIRCRAFT CONTROLLERS

Major Field: Mechanical and Aerospace Engineering

Biographical:

Education:

Completed the requirements for Master of Science in Mechanical and Aerospace Engineering at Oklahoma State University, Stillwater, Oklahoma in December, 2022.

Completed the requirements for Bachelor of Science in Aerospace Engineering at Oklahoma State University, Stillwater, Oklahoma in 2020.

Completed the requirements for Bachelor of Science in Mechanical Engineering at Oklahoma State University, Stillwater, Oklahoma in 2020.

Experience:

Autonomous Vehicle Software Engineer at Aurora Flight Sciences from October, 2022 - Present

Graduate Research Assistant for Dr. Imraan Faruque at Applied Physics Group, Oklahoma State University from June, 2021 to September, 2022.